Accepted Manuscript

Mineralogical controls on porosity and water chemistry during O_2-SO_2-CO_2 reaction of CO_2 storage reservoir and cap-rock core

Julie K. Pearce, Alexandra Golab, Grant K.W. Dawson, Lydia Knuefing, Carley Goodwin, Suzanne D. Golding

PII: S0883-2927(16)30414-0

DOI: 10.1016/j.apgeochem.2016.11.002

Reference: AG 3743

To appear in: *Applied Geochemistry*

Received Date: 19 October 2016

Revised Date: 31 October 2016

Accepted Date: 2 November 2016

Please cite this article as: Pearce, J.K., Golab, A., Dawson, G.K.W., Knuefing, L., Goodwin, C., Golding, S.D., Mineralogical controls on porosity and water chemistry during O_2-SO_2-CO_2 reaction of CO_2 storage reservoir and cap-rock core, *Applied Geochemistry* (2016), doi: 10.1016/j.apgeochem.2016.11.002.

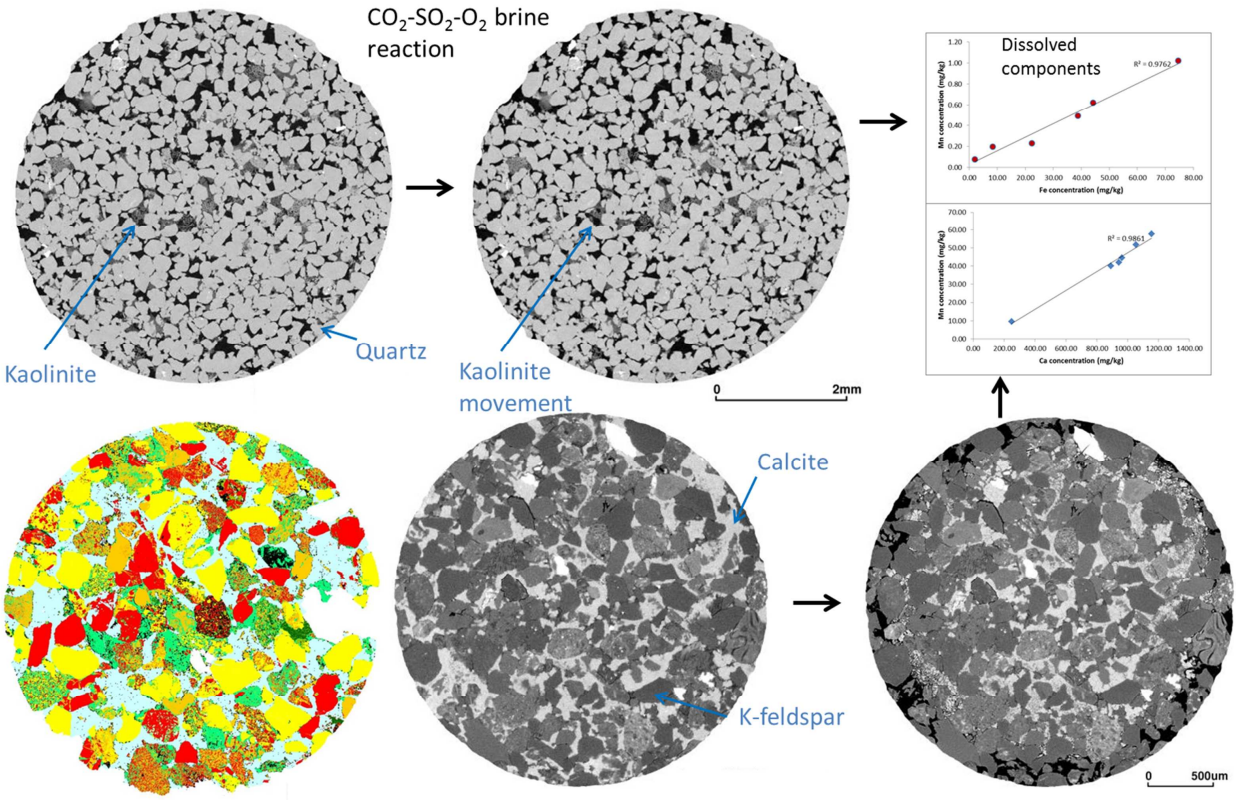

Mineralogical controls on porosity and water chemistry during O_2-SO_2-CO_2 reaction of CO_2 storage reservoir and cap-rock core

Julie K. Pearce[1*], Alexandra Golab[2], Grant K. W. Dawson[1], Lydia Knuefing[2], Carley Goodwin[2], and Suzanne D. Golding[1]

[1]*School of Earth Sciences, University of Queensland, St Lucia, Brisbane, QLD 4072, Australia*

[2]*FEI, Canberra, ACT 2600, Australia*

* *J.pearce2@uq.edu.au*

ABSTRACT

Reservoir and cap-rock core samples with variable lithology's representative of siliciclastic reservoirs used for CO_2 storage have been characterized and reacted at reservoir conditions with an impure CO_2 stream and low salinity brine. Mineralogical controls on the resulting changes to porosity and water chemistry have been identified. The tested siliciclastic reservoir core samples can be grouped generally into three responses to impure CO_2-brine reaction, dependent on mineralogy. The mineralogically clean quartzose reservoir cores had high porosities with negligible change, after reaction, in resolvable porosity or mineralogy, calculated using X-ray micro computed tomography and QEMSCAN. However, strong brine acidification and a high concentration of dissolved sulphate were generated in experiments owing to minimal mineral buffering. Also, the movement of kaolin has the potential to block pore throats and reduce permeability. The reaction of the impure CO_2-brine with calcite-cemented cap-rock core samples caused the largest porosity changes after reaction through calcite dissolution; to the extent that one sample developed a connection of open pores that extended into the sample. This has the potential to both favor injectivity but also affect CO_2

migration. The dissolution of calcite caused the buffering of acidity resulting in no significant observable silicate dissolution. Clay-rich cap-rock core samples with minor amounts of carbonate minerals had only small changes after reaction. Created porosity appeared mainly disconnected. Changes were instead associated with decreases in density from Fe-leaching of chlorite or dissolution of minor amounts of carbonates and plagioclase. The interbedded sandstone and shale core also developed increased porosity parallel to bedding through dissolution of carbonates and reactive silicates in the sandy layers. Tight interbedded cap-rocks could be expected to act as baffles to fluids preventing vertical fluid migration. Concentrations of dissolved elements including Ca, Fe, Mn, and Ni increased during reactions of several core samples. Precipitation of gypsum, Fe-oxides and clays on seal core samples sequestered dissolved elements including Fe through co-precipitation or adsorption. A conceptual model of impure CO_2-water-rock interactions for a siliciclastic reservoir is discussed.

KEYWORDS

CO_2 geological storage; sandstone reservoir; cap-rock, SO_2 impurities, O_2 impurities; CO_2-water-rock interactions; micro CT

1. INTRODUCTION

CO_2-water-rock reactions during CO_2 storage may not only affect water quality and mineralogy, but can also dynamically shape the pore and throat morphologies of the rock potentially changing porosity and permeability and hence fluid migration (Farquhar et al., 2015; Luquot et al., 2016; Navarre-Sitchler et al., 2013). Capture gas streams, from industrial processes such as coal fired power plants (e.g. post combustion capture or oxy-fuel processing), gas processing,

lime, steel, or cement production, sequestered subsurface can contain different concentrations and mixtures of impurity gases along with CO_2 (Porter et al., 2015; Talman, 2015). For coal combustion, depending on the combustion and capture system, concentrations of O_2 ranging from 0 – 5 % have been reported, with SOx concentrations of 0 – 70 ppm. SO_X concentrations up to 0.5 and 2.5% have been considered by authors as representative of capture from cement production or unprocessed flue gas (Last and Schmick 2011; Talman, 2015). The concentrations of SO_2 and O_2 in experiments were selected to represent an average of those suggested by literature. The majority of current capture techniques however require scrubbing of SO_X to low concentrations, for example <10ppm for MEA, hence re-addition of SO_2 to the CO_2 stream post purification may be necessary to attain higher concentrations. CO_2 streams containing impurity gases including SO_X, O_2, NO_X and H_2S have been identified as potentially more reactive than pure CO_2 to rock and well-bore materials (Jacquemet et al., 2008; Pearce et al., 2015a; Ruhl and Kranzmann, 2013; Wilke et al., 2012). The majority of experimental and geochemical modelling studies of CO_2-water-rock interactions, however, have used pure CO_2. Relatively few studies have presented experimental and modelling data with the presence of one or more impurity gases, and data for O_2 or NOx co-injection are extremely sparse (Pearce et al., 2016). SO_2 has been observed to acidify formation water, enhancing silicate dissolution, and also to reduce Fe^{3+} to Fe^{2+} making it available for mineral trapping as siderite or formation of sulphate minerals (Palandri and Kharaka, 2005; Pearce et al., 2015b). Some geochemical modelling studies have predicted strong acidification with SO_2 co-injection, however other studies have shown that the presence of carbonate minerals can buffer the pH (Kirste et al., 2016; Xu et al., 2005). O_2 has the potential to oxidize co-injected SO_2 or minerals such as pyrite, acidifying formation water, and also induce precipitation of oxide minerals (Jung et al., 2013; Lu et al., 2016; Lu et al., 2014;

Schaef et al., 2013; Shao et al., 2014). Changes to system redox potential through injecting CO_2 ($\pm$ SO_2, H_2S, O_2 or NO_X) can potentially mobilize elements such as Fe and Mn to solution or immobilize them in or on minerals such as siderite, Fe-oxides and hydroxides, these metals can be of concern if fluids migrate to drinking water aquifers or bores (Karamalidis et al., 2013; Marcon and Kaszuba, 2015). This higher reactivity of impure gas streams also has the potential to lead to benefits such as enhanced mineral trapping and remediation or self-sealing as long as potential negative impacts can be identified and mitigated. A reduction in capture and purification costs has also been suggested by avoiding, for example, SOx scrubbers and co-injecting SO_2 in certain situations (Glezakou et al., 2012; Xu et al., 2007). Capture cost reductions have recently been reported for CO_2 and H_2S co-injection at the Carbfix site.

Automated rock core analyses such as QEMSCAN (automated mineral analysis), 3D X-ray micro computed tomography (micro-CT) and Hylogger, are increasingly used for large scale characterization of core mineralogy and rock properties by the oil and gas industry and more recently for CO_2 sequestration sites (Farquhar et al., 2013; Golab et al., 2015b; Higgs et al., 2015). These data can be incorporated into larger scale site models to improve predictability of reservoir scale behavior, especially when combined with traditional methods such as X-ray diffraction (XRD) or mercury intrusion capillary pressure. A handful of studies have used micro-CT imaging or core scale CT imaging and QEMSCAN before and after pure CO_2-brine rock reactions, either coupled with water chemical analyses or geomechanical characterization including (Farquhar et al., 2015; Hangx et al., 2013; Luquot et al., 2016; Smith et al., 2013). The formation of wormholes in limestone or evaporite cap-rock core samples or dissolution of calcite and dolomite cements around quartz framework grains in siliciclastic core samples has been observed by CT in batch or flow through reactions. Fracture evolution and permeability

reduction through fines movement in fractured carbonate cap-rock has also been characterized by CT (Ellis et al., 2013; Ellis et al., 2011). The coupling of high resolution micro-CT imaging with QEMSCAN analysis and conventional scanning electron microscope energy dispersive spectra (SEM-EDS) allows the characterization, quantification and visualization of pores, throats and mineral distributions (Golab et al., 2015b). The further coupling of these rock characterization techniques with dynamic water chemical changes during gas-water-rock interactions reveals the reactions controlling pore network morphology, which can be linked to rock lithology and assist interpretation. The potential effect on water chemistry or mineral trapping can be assessed; in addition identifying the reaction of minor amounts of minerals not resolvable by rock characterization often necessitates identification through changes in water chemistry.

Several target sandstone reservoirs internationally have variable lithology, with similar reactive minerals to the study site including calcite and ferroan carbonates, chlorite, and plagioclase feldspars e.g. the Stuttgard Formation of the Ketzin site, Germany, the Archer Daniels Midland demonstration site, Illinois Basin, USA, or the Adventdalen Group, Norway (Alemu et al., 2011; Carroll et al., 2013; Fischer et al., 2013). Fe-rich chlorite has been observed in several sites including Ketzin and Krechba, Algeria, (Armitage et al., 2010).

Comparing the reactivity of cores of different lithologies often present in CO_2 storage reservoirs allows a broader understanding of potential changes to porosity, mineralogy, and water chemistry linked to lithology. The objective of this study was to determine the responses of different lithology cores to impure CO_2. Six representative lithologies of the quartzoze Precipice Sandstone, and calcite cemented or clay-rich Evergreen Formation and Hutton Sandstone core samples from a target low salinity CO_2 sequestration site in the Surat Basin, Australia, were characterized before and after reaction with a range of techniques. Core samples were reacted

with O_2-SO_2-CO_2-brine at reservoir conditions with periodic fluid sampling and analyses. A generalized conceptual model linking siliciclastic core lithology with changes to water chemistry, mineralogy, porosity and pore connectivity was developed.

2. METHODS

Six core sections from the West Wandoan 1 well drilled in the Surat Basin, Queensland, Australia, for a CO_2 storage feasibility study were tested. Two quartzose core sections from the reservoir unit, the Precipice Sandstone, sampled at 1217.48 and 1165.44 m depths, referred to as P1217m and P1165m were selected (note, after reaction the core samples or sub-plugs are referred to as e.g., P1217mR). Three core sections from the lithologically heterogeneous Evergreen Formation (cap-rock) sampled at 1056.10 m, 1043.70 m, and 981.24 m were reacted. Additionally one core sample from the overlying Hutton Sandstone at 800.83 m was also tested. The analytical techniques applied to the cores are summarized in Table A1.

The characterization of different core samples by a similar technique with 3D micro-CT and QEMSCAN have been described in detail previously (Farquhar et al., 2015; Golab et al., 2014). Briefly, whole core sections were first scanned by FEI HeliScan micro-CT at low resolution to select representative areas to core sub-plugs of 3 - 8 mm diameter that were subsequently imaged by FEI HeliScan micro-CT to produce tomograms at 1.7 – 5.1 µm voxel size. Core sub-plugs from the Evergreen Formation and Hutton Sandstone were 3 mm in diameter, with the Precipice Sandstone P1165m sub-plug 6 mm in diameter and P1217m sub-plug 8 mm in diameter. Voxel sizes were 1.7 µm for E1056m, 2.1 µm for E981m and E1043m, 2.3 µm for H800m, 3.7 µm for P1165m, and 5.1 µm for P1217m. Adjacent sub-plugs were also prepared for reaction with pure CO_2 as reported elsewhere (Dawson et al., 2015). A slice was trimmed from each sub-plug with a polished section prepared for higher-resolution 2D FEI Quanta FEG 650F SEM imaging and

FEI QEMSCAN analysis (Golab et al., 2015c; Golab et al., 2010; Knackstedt et al., 2013). This process was repeated after the sub-plugs were reacted, with the polished section taken from the same end of the sub-plug. The same end was used so that the two polished sections can be compared but differences could occur owing to minor vertical heterogeneities.

The pre and post reaction tomograms were then registered into perfect geometric alignment with one another to characterize changes caused during the gas-brine-rock interaction. The two 3D tomograms were also registered to the 2D SEM image mosaics and then to the 2D mineral maps from QEMSCAN. This allowed the characterization of µm-scale features, e.g. the 3D occurrence and distribution of heavy minerals, pores, cements, clay minerals and organic material. In the pre-reaction sub-plugs, sub-resolution pores (pores smaller than the given resolution) associated with clay minerals, weathered grains and/or diagenetic cements were characterized using a tomogram differencing technique described below and in Golab *et al.* (2010). Each sub-plug was first imaged by micro-CT in the dry state, then saturated with an X-ray dense brine (KCl) to highlight the connected pore space and re-imaged in the saturated state. The two tomograms were then registered into perfect geometric alignment and a difference tomogram was created by appropriately calibrating attenuation and then subtracting the registered tomograms. In this difference tomogram the greyscale values directly correspond to the volume of brine filling the connected porosity at each voxel. A voxel fully capturing a pore will have a value on one end of the grey scale spectrum, a voxel capturing a solid material, thus having no brine response at all will be at the other end of the grey scale spectrum. Since only the brine response is captured, the grey scale values of partially filled voxels will change linearly between those endpoints depending on their sub-resolution porosity.

This digital processing was followed by porosity segmentation to calculate and map the total effective porosity. For this purpose, each voxel within the images is designated to either represent resolved pores, solids, or the intermediate region, based on three-phase image segmentation. Subsequently, voxels segmented as resolved pores were assigned a 100% porosity value and those segmented as solid a 0% porosity value. All voxels of the intermediate region of the three-phase segmentation were binned based on their intensity. This allows representation of the porosity of each voxel from the greyscale value between 0% porosity and 100% porosity. This procedure allows the mapping and quantification of the total connected porosity averaged over the entire plug tomograms. Increases in the sub-resolution porosity caused by reactions were calculated from the decrease in X-ray density between the pre- and post-reaction tomograms. Other causes of changes in X-ray density between the pre- and post-reaction tomograms are Fe leaching from Fe-chlorite or movement of fines. On registering the post-reaction tomogram it was found that the Fe-chlorite had become less X-Ray attenuating but SEM images of it post reaction didn't show an increase in porosity. In the literature there are multiple references to Fe leaching of chlorite so it was assumed that the loss of X-Ray attenuation without an increase in porosity was due to leaching of Fe.

QEMSCAN™ is useful for gaining quantitative data on coarser grained rocks but on very fine grained or clay-rich lithologies it is less useful because the interaction volume is too large to allow the accurate identification of minerals. Hence, for very fine-grained material, the energy dispersive X-ray spectra collected for a given pixel may be a mix of multiple minerals, resulting in a component of unclassified or trace unidentified minerals.

Spot SEM-EDS was also performed on uncoated unpolished core blocks pre- and post-reaction with a JEOL JSM-6460LA environmental SEM fitted with a Minicup EDS, where the same

positions were analyzed pre- and post-reaction, where possible, to avoid ambiguity with previous diagenetic alteration. Unstressed nitrogen and 1500 mg/kg NaCl brine permeability of selected 15 mm core blocks was also measured pre and post reaction by a differential pressure technique using a linear fit applying the Klinkenburg correction (Dawson et al., 2015).

Adjacent core sections were subjected to whole rock fusion and elemental analysis by inductively coupled plasma optical emission spectroscopy (ICP-OES) to determine major elemental compositions of the core sub-samples reported as percentage oxides. Loss on ignition (LOI) was also determined, along with trace element analysis by HNO_3-HF-HCl whole rock acid digestion and analysis by Inductively Coupled Plasma Mass Spectrometry (ICP-MS) with an error less than 5% as described previously (Pearce et al., 2015b). The reacted core section of E1056mR was also analysed for minor and trace element content. E 1056R and precipitated material on H800mR were characterized by XRD post-reaction to identify any precipitates with a Bruker D8 Advance diffractometer.

Core sub-plugs and 15mm blocks were submerged in 100ml of deoxygenated 1500 mg/kg NaCl brine and reacted in unstirred, lined, reactors at 60° C and 12 MPa with a water-rock ratio of 10, with the reactors shown in Figure 1 (Pearce et al., 2015a). The reactors are based on unstirred Parr reactors with temperature control through a dedicated Labview interface. They are pressurized with an ISCO injection pump. Vessels and the fluid sampler system are fully lined in PEEK, with PEEK core sample holders to prevent contact of reaction fluids with the vessel. The E1056m rock sample was however reacted in a 1% KCl brine to prevent potential disaggregation by swelling clays. The reactors were first purged and pressurized with N_2, and after 3 days fluids were sampled, the reactors depressurized, and repressurized with a gas mixture of 2% O_2, 0.16% SO_2 and a balance of CO_2. Fluids were sampled periodically, with pH

and conductivity measured immediately ex situ (TPS WP81, error ± 0.01). Samples were filtered (0.45 µm), diluted 10 times, acidified with 2% HNO_3 and analysed by Inductively Coupled Plasma Optical Emission Spectroscopy (ICP-OES) with a Perkin Elmer Optima 3300DV, and error less than 5%. Unfiltered samples from the reactions of the cap-rock cores were also analysed by ICP-OES for total metals. Selected samples were filtered, diluted, acidified with ultrapure HNO_3 and analysed by ICP-MS. Sulphate was measured by ion chromatography (ALS Environmental, Brisbane, ± 1 mg/kg) and alkalinity by titration on selected unacidified samples. A blank experiment without rock was also performed to ascertain any baseline cations from the brine or minor reactor corrosion. After reaction rock blocks and sub-plugs were removed and oven dried at 60°C.

Experiments were modelled using the react module of Geochemist Workbench 9 (GWB) using experimental data as the initial water chemistry and mineralogical input to determine in situ pH and assist interpretation (Bethke and Yeakel, 2012; Delany and Lundeen, 1989). Input kinetic parameters and surface areas are described previously and are in the supporting material of this article (Pearce et al., 2015a).

3. RESULTS

3.1 Changes to core mineralogy and porosity

3.1.1 Precipice Sandstone

The Precipice Sandstone sections P1217m and P1165m of the WW1 well are quartzose with 2-3 area% pore filling kaolin as determined by QEMSCAN and traces of muscovite and rutile (Fig. 2a, Table 1). Both kaolinite and dickite polymorphs were identified in XRD of adjacent core

samples, both kaolinite and dickite were previously identified in Precipice Sandstone core from the Chinchilla-4 well (Dawson et al., 2015). P1165m was fine to medium grained, and P1217m course grained, friable and poorly sorted. At the core scale coarser grained horizontal layers were visible in P1217m. Micro-CT resolvable porosity of the sub-plugs is 20.9 % and 19.4 % for P1217m and P1165m respectively (Table 2a), in good agreement with 22 and 18.5% porosity respectively determined by mercury injection of adjacent core sections (Dawson et al., 2015). This is also in good agreement with helium porosities of Precipice Sandstone core samples from the same well reported elsewhere in the range 13.6 – 25% with the majority above 20% (Golab et al., 2015a). Trace minerals identified in the core blocks by SEM-EDS (and confirmed by XRD) included Na-carbonates, K-(Na)-sulphates (Fig. 3a, c), and calcite (Fig. 3c) in P1217m only. It is, however, possible that the K-sulphates originated from precipitated drilling fluids. Rhodochrosite, orthoclase and muscovite in trace amounts were identified in adjacent core sections of both core section depths in XRD. Ti-oxides (Fig. 3e), sporadic framboidal pyrite, and siderite were observed by SEM-EDS in both core depths. Fe-oxide laminations have been reported elsewhere in all cores, with Fe-oxides observed in P1165m via petrography. The core trace element contents are given in Table 3b, a high Ti concentration reflects the Ti-oxide content.

Post-reaction the trace amounts of Na-carbonates, K-sulphates, calcite and siderite dissolved in P1217m (Fig. 3b,d). Specks of precipitated oxides and sulphides containing Fe, Ni, Cr and S were observed on kaolinite post reaction. The decrease in calculated micro-CT resolvable porosity of P1165m was less than 0.5 % and attributed to dissolution of trace minerals and fines or clay movement (Table 2b). Movement of kaolinite was observed by both SEM on block surfaces (Fig. 3f) and when comparing pre and post reaction micro-CT images in both P1165m

and P1217m (Fig. 1S, supporting material). The brine permeability of P1165m decreased slightly from 294 mD to 277.5 mD post-reaction, and the N_2 permeability of P1217m increased from 1480.9 mD to 1650.5 mD (brine permeability of P1217m was above instrument range) (supporting material). The initial permeabilities are within the ranges of those measured with air and brine from various Precipice Sandstone core plugs from the same well reported elsewhere (Golab et al., 2015a). The air permeabilities were generally higher in the lower Precipice Sandstone, with a very low permeability in the cores measured around 1207 – 1212 m depth.

3.1.2 Evergreen Formation

The Evergreen Formation core E1056m is calcite cemented around quartz, plagioclase, and K-feldspar framework grains, with pore filling illite-smectite, and chlorite, kaolinite and muscovite (Fig. 2b, Fig. 4a), 25 area% calcite was quantified in the sub-plug slice by QEMSCAN (Table 1). The plagioclase was identified as both albite and calcium-rich labradorite in electron microprobe and XRD reported elsewhere with lesser orthoclase (Dawson et al., 2015). Apatite, Ti-oxide and coal are present in trace amounts (Fig. 5a), along with sporadic sphalerite and chalcopyrite. Micro-CT quantified 0.5% of possible organic content in E1056m. Higher major and trace element contents were generally present in all Evergreen Formation core samples compared to the Precipice Sandstone (Table 3), including Fe, Cr, Ni, V, Zn, and Li. After reaction, trace element content generally decreased slightly in E1056m core (supporting material). Micro-CT resolvable porosity was 0.6% in the sub-plug, but the image differencing technique yielded a porosity of 4.4% (Table 2a) (micro-CT image analysis of the sister sample used for pure CO_2 reaction yielded a higher porosity of 6.8%) (Golab et al., 2015c). Porosity determined by mercury injection capillary pressure analysis of an adjacent core sample was higher at 8.2 %

which may reflect core heterogeneity. E1056m contains ~11 % illite-smectite that could alternatively host sub-micron porosity in the range 3-4 nm. Brine permeability was below mD range. Helium porosity of a similar depth core sample from the same well (from 1056.24 m) has also been reported elsewhere at 6.8%, with helium porosities of Evergreen cores reported in the range 4.7 – 13.7 indicating significant variability with depth (Golab et al., 2015a).

Post-reaction, calcite cement was dissolved from E1056mR, with a reduction of 9 area% calcite in the sub-plug polished section (Table 1), and porosity was created extending into the center of the sub-plug (Fig. 4a,b,c). High resolution SEM images of polished slices through the sub-plug show calcite dissolution at the edges leaving residual framework silicate grains and clays. In the center of the sub-plug calcite cement remains but contains channels through pre-existing micro fractures in the calcite cement (Fig. 3S, supporting material). The change in tomograms after reaction was 9.1% (Table 2b), which includes porosity changes from mineral dissolution but potentially also small changes from fine particle movement, Fe-leaching from chlorite or slight misalignment of tomograms. Pore-filling clay was revealed by calcite dissolution potentially hosting sub-micron porosity (Fig. 5a). Silicates and Ti-oxide grains showed little to no corrosion. Barite crystals were precipitated on the core block surface, with Ca-sulphate precipitated in the reactor (Fig. 5c-f). Illite/muscovite content determined by QEMSCAN increased post-reaction (Table 1) indicating potential precipitation of illite (or heterogeneity caused by the use of a different polished section before and after reaction). Semi quantitative XRD of the core block after reaction was in reasonable agreement with QEMSCAN and did not indicate detectable substantial mineral precipitation (supporting material).

E1043m is a fine-grained sandstone and E981m an interlaminated sandstone and siltstone (Fig. 2c,d, Fig. 4d). Sub-plugs of E1043m and E981m contain 3.8 and 7.6 % chlorite that is Fe-rich

298 (Table 1, Fig. 6a). SEM-EDS also indicated E1043m contained trace calcite, gypsum, and
299 sphalerite with some plagioclase Ca-rich (Fig. 6a). E981m contained trace fine-grained ankerite
300 (and possibly siderite) associated with the chlorite (Fig. 7a). E1043m contained 4.4 % possible
301 organic content calculated from the tomograms, and E981m 1.1 % possible organic content.
302 Along with coal, trace minerals in both E1043m and E981m include barite, apatite, Ti-oxide,
303 (REE,U)-monazite (Fig. 6E), zircon, sphalerite, Cu-pyrite. Trace FeO(OH) (lepidocrocite) was
304 also identified in adjacent sections of E1043m by XRD reported elsewhere (Dawson et al.,
305 2015). The E1043m sub-plug has a porosity of 6.3 % from micro-CT analysis, and E981m 8.3
306 % (Golab et al., 2015c). This is in good agreement with mercury injection porosities of 5.5 and
307 8.4 % respectively measured for adjacent core blocks. A similar depth core sample (1043.72 m)
308 was also characterized elsewhere by helium porosity at 7.6% (Golab et al., 2015a). E981m also
309 contains ~23% illite-smectite that could potentially host sub-micron porosity in the range 3-4
310 nm. Brine permeabilities were below the mD range measured.
311 After reaction, remaining chlorite had a reduction in X-ray density in both sub-plug tomograms
312 with in some cases no created porosity indicating a reduction in Fe content in the chlorite (Fig.
313 4e,f). Chlorite also appeared to have a reduction in Fe content in separate SEM-EDS analysis.
314 Trace carbonates, calcite and ankerite, were also dissolved (Fig. 6b, and 1Ssupporting material),
315 with more visible changes to the sandy section of E981mR (Fig. 4f). K-feldspar and Ca-rich
316 plagioclase grains were observed in SEM to be corroded (Fig. 6c, d, 7 c, d) along with sphalerite
317 and phosphate (Fig. 6b,f). Fine grained precipitated material covered areas of the core samples
318 including silica booklets on pre-existing K-feldspar in E1043 m (Fig. 6d). Both core samples
319 were covered by precipitated barite, and Fe rich oxides and clays (Fig. 6d). Trace barite was also
320 identified in QEMSCAN in E1043mR although this may have been present pre-reaction (Fig. 4S,

supporting material). The QEMSCAN determined kaolinite content slightly increased post reaction in both E1043mR and E981mR. The micro-CT calculated change in porosity after reaction of E1043m was 3.5%, and of E981mR was 3 %. The calculated increase includes density changes from Fe leaching of chlorite or loss of fines. Apparent created, horizontally connected, porosity is visible in the sandy layer of the E981mR sub-plug (Fig. 4e,f), with created porosity or density changes otherwise appearing disconnected in the shaley section of E981mR (Fig. 4f), and also in E1043mR (Fig. 1S, supporting material). Brine permeability did not measurably increase in E1043mR.

3.1.3 Hutton Sandstone

H800m is highly calcite cemented around quartz and feldspar framework grains with some pore filling kaolinite, and coal laminations (Fig. 2e, Fig. 8a). The sub-plug polished section contained 37 % calcite, with also muscovite/illite, chlorite, plagioclase and biotite identified by QEMSCAN (Table 1, Fig. 8c). Plagioclase was identified as a mixture of albite and Ca-Na-plagioclase by XRD, and trace Ca-phosphate was observed in SEM-EDS of the core blocks along with sphalerite. Occasional REE, U-monazites and pyrite/FeS were reported in adjacent core sections (Dawson et al., 2015). Trace metal content is generally higher than in the Precipice Sandstone core samples including Sr, Ba, Zn, P along with the major Ca oxide content (Table 3). Micro-CT image analysis porosity is 3.8 % (and micro-CT image analysis of the sister sample used for pure CO_2 reaction yielded a higher porosity of 5.2%) (Golab et al., 2015 Appendix B). Porosity determined by mercury injection capillary pressure analysis of an adjacent core sample was 6.7 %. The brine permeability was below mD range (recent measurements of other sections

of this core have μD range permeability), with vertical N_2 permeability of 0.2 mD (supporting material).

Calcite cement dissolved and Ca-sulphate crystals with a gypsum morphology were visibly precipitated over the H800mR core samples post reaction (Fig. 8b,e,f). The precipitated crystalline material was analyzed by XRD confirming its identity as gypsum. A loss of 18% calcite was calculated from the two sub-plug polished sections by QEMSCAN analysis (Table 1), with an 8.4 % increase in kaolinite content indicating kaolinite precipitation (or heterogeneity caused by the use of a different polished section before and after reaction). Fine-grained precipitates with an EDS signature indicating kaolinite were also observed. Although gypsum was precipitated over the surface of the sub-plug, most crystals broke off in transit and preparation for post-reaction characterization, with QEMSCAN only detecting 0.2 area% gypsum (supporting material). Phosphates were corroded, and fine-grained cubic precipitates (~5 μm) also covered some silicates (Fig. 8d). Calcite dissolution appeared mainly around the edges of the H800mR sub-plug with created porosity less extensive (Fig. 1S, supporting material) than in the calcite cemented E1056mR sub-plug. The micro-CT calculated change in porosity after reaction was 3.7% in the H800mR sub-plug, less than the porosity increase in the calcite cemented E1056mR (Table 3b). The core N_2 permeability also increased to 4.5 mD.

3.2 Water Chemistry

3.2.1 Precipice Sandstone

Solution pH decreased from 4 - 5 during the N_2-brine-rock soak of P1217m and P1165m (with an alkalinity of 43 mg/kg as $CaCO_3$), to a minimum of pH 1 after O_2-SO_2-CO_2 gas injection, and was subsequently buffered to a maximum of 1.8 (Table 4, Fig. 9a). Dissolved element

366 concentrations in solution were generally low (Table 4a, b), except Fe increased to 75 mg/kg
367 during reaction of P1165m and subsequently decreased to 39 mg/kg (Fig. 9c), and K increased to
368 195 mg/kg during reaction of P1217m. Solution electrical conductivity increased to a maximum
369 of 11 ms/cm during reaction of P1217m, and 34 ms/cm on reaction of P1165m subsequently
370 decreasing to 13 ms/cm. Sulphate concentration increased from 193 mg/kg to 1613 mg/kg at 72
371 h, 1493 mg/kg at 216 h, and decreased to 607 mg/kg at 696 h during reaction of P1217m, and
372 increased from 21 mg/kg to 1507 mg/kg at 672 h for P1165m. Cr concentration reached 16
373 mg/kg during reaction of P1165m but subsequently decreased. Trace concentrations of dissolved
374 P were also detected in reaction of P1165m (Table 5).Calculated in situ pH was in excellent
375 agreement, decreasing sharply to 1.8 for P1217m, and for P1165 to 1.5 (Fig. 5S, supporting
376 material). Several minerals were saturated including nontronite, and also hematite which
377 precipitated in P1165m.
378
379 ***3.2.2 Evergreen Formation***
380 During reaction of E1056m, pH initially decreased slightly but was subsequently buffered by the
381 dissolution of calcite cement to 6.3 (Fig. 9a, Table 4), initial alkalinity was 110 mg/kg as $CaCO_3$,
382 and conductivity increased. Dissolved element concentrations were high compared to Precipice
383 core reactions, with Ca concentration initially increasing rapidly then gradually to 1156 mg/kg,
384 Mn to 56 mg/kg, Mg to 9 mg/kg and Ni to 29 mg/kg after 624 h reaction (Fig. 9b). Fe, Al and
385 Si, however, remained at low concentrations, with dissolved total S increasing to 387 mg/kg
386 (Fig. 9c, d, Table 4). Unfiltered samples of all Evergreen core reactions were also tested for total
387 metals (Table 2S, supporting material); generally concentrations were comparable within error to
388 filtered waters, with some elevated concentrations of Fe in all and also Cr in the case of E1056 m

389 reaction indicating either some Fe-rich clay fines or Fe-rich precipitates larger than 45 µm
390 present in solutions. The total concentration of P in Evergreen reactions was also highest from
391 E1056m, likely from apatite dissolution. Calculated in situ pH was stable at ~5 (Fig. 5S,
392 supporting material), calcite dissolution dominated with predicted dissolved Ca concentration
393 slightly low (Fig. 7S, supporting material). No precipitation or saturation of gypsum or
394 anhydrite was predicted (Fig.7S, supporting material); however glauconite, nontronite, hematite
395 and jarosite were saturated.
396
397 Solution pH sharply decreased and was subsequently slightly buffered to 2.3 during reaction of
398 E1043m and E981m (Fig. 9a, Table 4). Conductivity increased and subsequently decreased by
399 the end of experiments. Concentrations of dissolved Ca, Mg, K, Na increased (Fig. 9b, Table 4),
400 Fe increased and subsequently decreased after ~ 200 h during both reactions, with Al
401 concentration increasing and subsequently decreasing during reaction of E1043m only (Fig.
402 9c,d). Fe, Al, Si and Li concentrations were generally higher than during reaction of other rock
403 cores. Initial alkalinity during the E1043m reaction was 155 mg/kg, with sulphate concentration
404 increasing from 5 to 1709 mg/kg at 648 h reaction. Cr concentration reached 23 mg/kg and
405 subsequently decreased to 7.6 mg/kg during reaction of E1043m, but remained below 2.9 mg/kg
406 from E981m. The concentration of Zn was relatively high from both cores (Table 4b).
407 Dissolved P was measured during reaction of E1043m, its concentration was initially high (Table
408 5). Analysis of unfiltered waters indicated P increased during reaction of both E1043m and
409 E981m (Table 2S, supporting material). Total Fe and K concentrations were higher in unfiltered
410 waters potentially indicating some fines or micron sized precipitates (e.g. potentially jarosite or
411 alunite) (Table 2S, supporting material). Calculated in situ pH was in excellent agreement with

412 the E1043m experiment decreasing to 1.8 and buffering slightly to 2.7 by model terminations.
413 Chlorite, plagioclase, and calcite were the main minerals dissolving and contributing to Ca, Fe,
414 and Al in the models. Calculated pH increased from 1.9 to 3 in good agreement with
415 experimentally measured pH during reaction of E981m (Fig. 5S, supporting material). Chlorite,
416 calcite, siderite/ankerite and K-feldspar were the main minerals predicted to dissolve, with
417 nontronite, hematite, glauconite, and jarasite saturated. Predicted precipitation of alunite
418 controlled dissolved Al concentration in modelled reaction of E1043 m.
419
420 ***3.2.3 Hutton Sandstone***
421 Solution pH during reaction of H800m decreased from 6.4 to 5.6 after O_2-SO_2-CO_2 gas
422 injection and was subsequently buffered to 5.9 by calcite dissolution, while electrical
423 conductivity increased from 3.7 to 5.4 ms/cm^3 (Fig. 9a, Table 4). The initial alkalinity
424 was 99 mg/kg as $CaCO_3$, with sulphate concentration increasing from 4 to 1251 mg/kg at
425 72h, 927 mg/kg at 216 h, to 1077 mg/kg after 696 h. Ca concentration increased rapidly
426 from 302 to 1039 mg/kg after 384 h, and then gradually decreased to 965 mg/kg after 696
427 h, Mn also increased to 32 mg/kg after 384 h then decreased slightly to 31 mg/kg after
428 696 h (Fig. 9b, Table 4). Dissolved Al, Si, and Mg concentrations remained relatively
429 low, with Fe, Ni, and Zn increasing and subsequently decreasing by 696 h reaction.
430 Calculated in situ pH was initially 4.2 decreasing to 3.5 then rapidly buffered to 4.8
431 (supporting material), with kaolinite and gypsum/anhydrite precipitated. Nontronite,
432 hematite, glauconite and jarosite were also saturated.
433
434 **4. DISCUSSION**

435

436 ***4.1 Quartzoze cores***

437 The quartzose reservoir core samples from the Precipice Sandstone have a relatively high
438 porosity calculated from micro-CT image analysis in good agreement with that determined by
439 mercury injection and indicative of a suitable storage reservoir. The relatively low reactivity
440 with O_2-SO_2-CO_2-brine indicates a low likelihood of plugging by precipitation; however,
441 kaolinite movement was observed which has the potential to plug pores and reduce permeability.
442 The movement of kaolinite was also observed in similar core samples on pure CO_2 reaction
443 indicating it is not specific to co-injection of SO_2 and O_2 gas (Golab et al., 2014). The
444 conversion of SO_2 to sulphuric acid resulted in a low pH that was not buffered in the absence of
445 significant reactive mineral phases, with high concentrations of dissolved sulphate. The
446 oxidation of trace amounts of sulphides present in core samples potentially also contributed to
447 the lower pH. Geochemical modelling of SO_2 co-injection in siliciclastic US Gulf aquifers
448 predicted acidification to pH values as low as zero (Xu et al., 2007). Recent reactive transport
449 modelling, however, indicates trace amounts of calcite in the Precipice Sandstone can buffer
450 acidity from co-injection of SO_2 with CO_2 (Kirste et al., 2015).
451 Dissolution of reactive minerals present in trace amounts in Precipice Sandstone core samples
452 including carbonates, clays and K-Al-sulphate resulted in dissolved major elements in solution at
453 generally low concentrations compared to other rock types, except Fe and K. Although
454 dissolved Fe was generally high, its concentration followed a decreasing trend. Dissolved Fe and
455 K were also elevated on pure CO_2 reaction of similar core samples although at around 7 and 10
456 times lower concentrations respectively than with impure CO_2 (Dawson et al., 2015). The
457 dissolved concentrations of minor elements including Zn and Cr were elevated (maximum of 4

458 and 16 mg/kg) during O_2-SO_2-CO_2 reactions of Precipice Sandstones core samples even though
459 the rock content of these elements was low relative to other rocks. Dissolved Ni and Cr however
460 decreased, and were observed in Fe-oxides precipitated on kaolin indicating a sink for these
461 metals. Sulphide minerals which were observed in trace amounts in the core samples have been
462 suggested to be a potential source of dissolved Cu, Zn, Ni or Cr in other rocks (Lu et al., 2014).
463 Oxidation of 0.7 wt% pyrite was linked to mobilization of Zn from Cardium Sandstone in O_2-
464 CO_2-brine reactions with 3.5% O_2 (Lu et al., 2014). A high dissolved Zn concentration on
465 reaction of P1217 m indicates the possible oxidative dissolution of trace sphalerite contributing
466 to minor or trace metals. The reaction of pyrite in the model also improved the match to
467 experimental Fe concentrations. The predicted in situ pH was in good agreement with
468 experiments for the quatzoze core reactions. The low pH was controlled by sulphuric acid which
469 did not degass on experimental sampling resulting in the good agreement. It should be noted
470 however that the very low pH generated in the Precipice Sandstone experiments is not expected
471 in the field where pH is often buffered by groundwater alkalinity, and any co-injected gases
472 would be at lower concentrations. Reaction of impure CO_2 with quartzoze cores had a greater
473 impact to pH than reaction with pure CO_2 by ~ 3 units. However the lack of reactive silicates
474 present meant that the changes to the rocks by mineral dissolution were the same. The Fe
475 concentration decreased toward the end of the O_2-SO_2-CO_2 reactions indicating a trace of
476 mineral precipitation. Hematite precipitation was predicted in the geochemical model of
477 P1165m. Allowing hematite precipitation however resulted in an under prediction of dissolved
478 Fe compared to the experiment through an over prediction of the amount of hematite
479 precipitated. The rate of hematite precipitation used was the same as the rate of dissolution

given the lack of data for mineral precipitation rates, modifying the nucleation rate improved the prediction but this highlights the need for mineral precipitation data.

4.2 Calcite cemented cores

The O_2-SO_2-CO_2 reactions of calcite cemented core samples were dominated by calcite dissolution with relatively large increases in porosity and N_2 permeability after reaction. The pH was quickly buffered preventing significant silicate mineral dissolution. Gypsum was precipitated on the H800m core sample from reaction of dissolved sulphate (from SO_2) with Ca from dissolved calcite. Kaolinite also precipitated along with small cubic crystals of an unknown mineral, potentially re-precipitated calcite. Precipitated gypsum was also observed in previous experiments reacting SO_2-CO_2 with calcite cemented Hutton Sandstone or siderite-ankerite minerals (Pearce et al., 2015a; Pearce et al., 2015b). Elsewhere basalts reacted with an O_2-SO_2-CO_2 gas mixture (1 wt% of each impurity) resulted in gypsum and also jarosite-alunite precipitation (Schaef et al., 2014). Precipitation of gypsum has also been observed in fractured limestone cores, marl cap-rock, and carbonate cemented sandstones reacted with CO_2 and sulphate rich brines (Dávila et al., 2016; Garcia-Rios et al., 2015; Luquot et al., 2016). The increase in sub-plug porosity from the H800 m sub-plug was 3.66% in the presence of SO_2 and O_2 where gypsum precipitated, with dissolution of 18.2 area % calcite cement from the analyzed slice (Appendix A2). The increase in porosity during pure CO_2 reaction however was almost double that at 6.1 %, with no mineral precipitation (Golab et al., 2015c). The precipitated gypsum during impure CO_2 reaction may have armored the core from further calcite dissolution. The armoring of dissolving carbonates dolomite and ankerite by precipitated gypsum has been suggested elsewhere to prevent significant carbonate dissolution (Luquot et al., 2016). The

503 precipitation of gypsum was also linked to decreased permeability at low flow rates in reactions
504 of fractured limestone with CO_2 and sulphate rich brine (Davila et al., 2016).
505 During reaction of the calcite cemented sandstone samples H800m and E1056m, the buffering of
506 pH resulted in minimal silicate dissolution and relatively low concentrations of associated
507 dissolved elements including Fe and Al. Initially elevated concentrations of dissolved Ni, Zn
508 etc. during reaction of H800m subsequently decreased and this was likely due to co-precipitation
509 of those cations with gypsum.
510 A more extensive porosity increase of 9.11% occurred through the E1056m sub-plug from the
511 lower Evergreen Formation during reaction (in 1% KCl brine) than the 3.7% porosity increase in
512 H800m. Gypsum was predicted to be unsaturated at the higher salinity hence did not precipitate
513 on E1056m or armor dissolving calcite. Dissolution of 9.2 % calcite was quantified from the
514 sub-plug slice. This agrees well with dissolution of 10.8% calcite calculated by mass balance
515 from the measured dissolved concentration of Ca in the experiment. The extensive dissolution of
516 calcite cement uncovered pore filling clays that could potentially lead to fines migration and
517 blocking of pore throats. Several flow through studies reacting pure CO_2 saturated brine with
518 fractured calcite cemented cores also observed carbonate dissolution leaving skeletons of
519 framework silicate grains or clays (Ellis et al., 2013; Ellis et al., 2011). Ellis and co-workers
520 observed fines migration of exposed silicates causing mechanical closure of the fractures or
521 permeability reduction. Compared to the pure CO_2 reaction of E1056m with a porosity increase
522 of 6.73% in the sub-plug, during impure CO_2 reaction the increase in porosity was greater at
523 9.11%.
524 In the current experiments, traces of barite also precipitated likely due to its insolubility during
525 depressurization. Dissolved Mn concentration was correlated with Ca (R^2 of 0.91) from

526 dissolution of the E1056m calcite cement. Mn remained high and increased, although this was
527 also the case during pure CO_2 reaction of the sister core sample (Dawson et al., 2015). The
528 concentrations of Zn and Sr were also correlated with Ca with R^2 of 0.84 and 0.81 respectively
529 and likely were sourced mainly from dissolution of calcite cement. Assuming all Ca, Mn and
530 Mg came from calcite, using molar ratios of dissolved concentrations indicates a Ca : Mn : Mg
531 content of 1 : 0.06 : 0.004 in the E1056m calcite. For calcite cemented cores, changes to pH and
532 water chemistry were similar with impure and pure CO_2, mineral precipitation was however only
533 observed with impure CO_2 reaction.
534 Regarding the geochemical models, published kinetic and thermodynamic parameters for the
535 minerals could sufficiently predict the experimental water chemistry. The reactive surface areas
536 of calcite cement however had to be decreased by a factor of 100 from 10 to 0.1 cm^2/g to match
537 the experimentally observed concentration of Ca from the dissolution of calcite. The occurrence
538 of calcite as a pore filling cement and the reaction of the majority of the material as solid core
539 blocks (larger than the sub-plug) would restrict the access of reactive fluids justifying the lower
540 surface area. The lowering of calcite surface areas is consistent with the work of (Kirste et al.,
541 2015; Pearce et al., 2015a). Surface areas of clays did not need increasing, likely owing to their
542 being mostly covered by the calcite cements. The use of published kinetic and thermodynamic
543 parameters is also consistent with the work of (Carroll et al., 2013) who found only small
544 adjustments to parameters were needed to fit their model output to experimental results.
545 ***4.3 Clay-rich cores***
546 The calculated porosity of clay-rich interlaminated shale and fine-grained sandstone core
547 samples E981m and E1043m increased slightly after reaction. However, micro-CT images show
548 that changes are generally mainly disconnected (rather than connected porosity generation) from

549 localized dissolution of carbonates and also silicates including labradorite, with density changes
550 from Fe-leaching of chlorite. Increases in porosity were greater after O_2-SO_2-CO_2 brine reaction
551 of E981m and E1043m (increase by 3.04 and 3.54% respectively) with the lower pH than
552 equivalent pure CO_2 reactions (an increase by 2.01 and 2.74% respectively) (Golab et al., 2015).
553 Some horizontally connected porosity created through the sandy layer of E981m after O_2-SO_2-
554 CO_2 brine reaction indicates CO_2-rich brines could migrate horizontally (baffle) under shales
555 encouraging residual and mineral trapping and reducing the likelihood of vertical migration
556 through the cap-rock. Further reactive transport modelling with batch and flow through
557 experiments at expected injected gas stream compositions (including NOx) would be needed to
558 confirm this.
559 Dissolved concentrations of Fe, Al, Mg, Li, Na, and K were high relative to other rock types
560 from the dissolution of trace carbonates, chlorite and labradorite owing to the lowered pH. The
561 concentration of dissolved Al from the shaley E981m sample was ~ 8 – 15 times higher than on
562 reaction of the Sandstones P1165m and P1217m. Dissolved Fe from E981m was also higher at 3
563 – 10 times that mobilized from P1165m and P1217m. This is consistent with the observation of
564 10 and 4 times more Al and Fe respectively from the Eau Claire shale than the Mount Simon
565 Sandstone during CO_2 reaction by (Carroll et al., 2013).
566 Dissolved Mn was relatively high in concentration from impure CO_2 reaction of E1043m with
567 Ca and Mn correlated with an R^2 of 0.99 up until 384 h reaction indicating a similar source.
568 Dissolved Zn and Ca were also somewhat correlated with an R^2 of 0.83 suggesting traces of
569 carbonates as the main source of Zn, however a contribution from oxidation of sphalerite may
570 contribute to the non-linearity. After 384 h, the non-linearity is possibly also from incorporation
571 of Ca into precipitated gypsum. During reaction of E1043m an increase in Co and Ni ~ 550 h

coincides with the later increase in Fe and Cr indicating a contribution from oxidative dissolution of sulfides. During reaction of E981m, Mn and Ca were correlated (R^2 0.997), along with Mg and Ca (R^2 0.99), Zn and Ca (R^2 0.97), and Sr and Ca (R^2 0.97). Ca/Mn ratios were similar during reaction of E981m and during 0 to 384 h reaction of E1043m indicating similar Mn contents of dissolving calcite or ankerite.

Compared to the pure CO_2 reaction of E981m, with impure CO_2 8 times more Fe and 15 times more Al was mobilized from silicates and available for mineral trapping. On reaction of impure CO_2, 20 times more Fe and 4 times more Al from E1043m was measured than with pure CO_2. High concentrations of dissolved Fe and Al in both impure CO_2 reactions subsequently decreased or stabilized through the precipitation of fine grained Fe-oxides and silicates observed on core samples along with traces of barite and gypsum. Mineral precipitation was not observed in equivalent pure CO_2 reactions. Geochemical models predicted Fe and Al were mainly from dissolution of chlorite, with saturation of Fe-oxides (hematite) and smectite (nontronite), although gypsum/anhydrite was not saturated. The high concentration of dissolved Fe may have encouraged a small amount of gypsum precipitation as has been reported elsewhere (Luquot et al., 2016). Relatively high dissolved concentrations of Ni and Zn reflect the relatively high contents of Ni and Zn present in the rock cores. Both Ni and Cr concentrations (Cr was highest from E1043m), however, decreased at the end of experiments, incorporated into precipitated oxide minerals with Ni and Cr signatures observed in EDS. This is in agreement with a separate study that observed precipitated secondary Fe-oxides to incorporate minor metals on reaction of CO_2 saturated brine with co-injected O_2 with Eau Clair shale (Shao et al., 2014). Carbonates can contain metals substituted into their structure such as Mn, Zn, Co, Ni that may be mobilized by dissolution. These have been noted by several authors as a potential concern to drinking water

595 sources if CO_2 migrates (Wunch et al., 2013,2014). The release of metals to solution is
596 dependent on the mineralogy of the rock. We observe similar magnitudes of release of Mn from
597 calcite with either pure or impure CO_2 reaction. Higher concentrations of Ni, Cr and Zn were
598 initially released from clay rich cores containing carbonates with impure CO_2 than with pure
599 CO_2, the concentrations however subsequently decreased. The presence of O_2 allows additional
600 oxidative dissolution of sulphides but also the precipitation of Fe-oxides which incorporate
601 metals. Understanding the sources and sinks of metals in different redox conditions requires
602 further work.
603 The E1043m core sample also had the highest rock content of P, with phosphates (rimming
604 zircon) observed in SEM. The phosphates dissolved during the experiment, with increasing total
605 concentrations of P measured in solution. Clay-rich cores had larger changes in porosity with
606 impure CO_2 than pure CO_2 as the lowered pH resulted in silicate dissolution. Changes however
607 appeared overall mainly in disconnected porosity or horizontal porosity unlikely to result in
608 vertical migration of CO_2.
609 Geochemical models required increases to the reactive surface areas of chlorite and illite clays by
610 a factor of 50 from 70 to 3500 cm^2/g to agree with experimental water chemistry. This reflects
611 the fine-grained nature of the clays containing observable porosity (supporting material) and lack
612 of coating by carbonate cements in the two clay-rich cap-rocks. Increasing the input surface
613 areas of reactive clays, especially Fe-rich clays in geochemical models is consistent with other
614 work where surface areas were increased up to 7000, 15000 – 100000, or 17000 – 74000 cm^2/g
615 for core blocks or fragments respectively (Carroll et al., 2013; Farquhar et al., 2015; Kirste
616 personal communication).

Further work is needed to understand the sources, mobilization and sinks of minor and trace metals and metalloids in CO_2 storage environments. Coal was present in several of the cores and has the potential to mobilize adsorbed elements or organic compounds (e.g. BTEX), this was not investigated and generally requires further work. The dissolution of carbonate cements uncovering clays, and the precipitation of minerals armoring carbonates from dissolution or covering silicate surfaces cause dynamic changes to mineral reactive surface areas one of the parameters with the largest uncertainty in modelling. Understanding these dynamic changes also warrants further work which would improve longer term geochemical modelling predictions.

5. CONCLUSIONS

The interaction of O_2-SO_2-CO_2-brine with six sandstone and shale core samples of variable lithology resulted in a mainly mineralogical control on porosity and major water chemistry changes. Conceptually the reactivity of the cores showed three types of behavior. Previous geochemical modelling has shown for example very extreme acidification with impure CO_2 which could corrode the wellbore, however the presence of carbonate minerals can buffer the pH. Here we have shown a range of resulting pH's 1-2, 3-4, and 6-8 depending on core lithology. Mineralogically relatively clean quartzose reservoir rock core samples had the least change in porosity, with minimal mineral dissolution indicating a good reservoir rock. The lack of reactive minerals resulted in the lowest solution pH and high concentrations of dissolved sulphate during experiments. Movement of pore-filling kaolin was observed which could potentially block pores and affect permeability, although the content of pore-filling minerals (predominantly kaolinite) is generally quite low in the Precipice Sandstone. In contrast,

carbonate-cemented core samples showed the largest increases in porosity through calcite dissolution over experimental timescales, with pH buffered to the highest values. Silicate mineral dissolution was therefore minimal with water chemistry dominated by ions from calcite dissolution. Subsequent precipitation of sulphate minerals and kaolinite decreased dissolved ion concentrations and has the potential to decrease or re-seal porosity over time. Reactive clay-rich cap-rock cores with small quantities of carbonates and plagioclase had small increases in what appeared to be disconnected porosity. for the interlaminated shale also showed some increased horizontal porosity in sandy sections. Reaction of the Fe-rich clays, plagioclase and carbonates buffered pH to relatively intermediate values. Water chemistry was dominated by ions from Fe-rich clays, plagioclase and carboante dissolution. For shales, sub-micron porosity can be significant and the use of techniques such as small angle neutron scattering (SANS) would be useful to estimate nanoscale porosity in future. The reaction of trace amounts of minerals including carbonates and sulphides (or potentially organic matter) contributed to dissolved metals and metalloids in solution. Several of these metals subsequently were sequestered or adsorbed with the precipitation of oxide, sulphate or silicate minerals especially on more reactive cap-rock core samples. However several dissolved metals continued to increase in concentration especially when pH was not significantly buffered. The sources, mobilization, and fate of metals which have the potential to affect fresh-water aquifers require further understanding.

Conceptually the injection of a CO_2 stream into a quartzose reservoir sandstone under layers of rock of variable relatively low porosity and permeability represents an optimized storage complex. The high porosity Precipice Sandstone has a low reactivity indicating a good injection target with a low likelihood of porosity clogging by mineral precipitation. Acidic fluids interacting with the base of reactive rock containing carbonates would likely be pH buffered with

663 dissolution of plagioclase and Fe-rich clays resulting in subsequent long term mineral trapping,
664 mainly as siderite or ankerite. Calcite cemented sections at the reservoir-seal interface represent
665 higher potential for initial porosity increases through calcite dissolution and horizontal
666 movement of fluids. In the presence of SO_2 and O_2, however fast precipitation of sulphates such
667 as gypsum and oxide minerals at reservoir - reactive seal rock interfaces have the potential to
668 seal porosity and sequester mobilised metals. Fluids could be expected to move horizontally
669 under low permeability clay-rich sections of the Evergreen Formation encouraging residual
670 trapping. Interbedded sandstones and shales can be expected to act as baffles to fluids,
671 decreasing the likelihood of vertical migration of CO_2 or CO_2 charged fluids.
672
673
674 **6. ACKNOWLEDGMENTS**
675 The authors wish to acknowledge financial assistance provided through Australian National Low
676 Emissions Coal Research and Development (ANLEC R&D). ANLEC R&D is supported by
677 Australian Coal Association Low Emissions Technology Limited and the Australian Government
678 through the Clean Energy Initiative. The technical assistance of Dean Biddle, Alison Law, and
679 Marietjie Mostert are acknowledged. The authors acknowledge the SEM facilities and scientific
680 and technical assistance of the Australian Microscopy and Microanalysis Research Facility at the
681 Centre for Microscopy and Microanalysis, University of Queensland. The authors thank CTSCo
682 and Dr. Rob Heath for access to core material, data and guidance. Dirk Kirste is also thanked for
683 providing kinetic rate scripts and helpful discussions. Two anonymous reviewers provided
684 feedback which greatly improved this manuscript.
685

7. APPENDIX A

8. SUPPLEMENTARY MATERIAL

Supporting material includes micro-CT tomograms E1043m, H800m, and P1165m, high resolution SEM images, select post-reaction QEMSCAN, a table of core permeabilities, table of total metals in solution during reaction, geochemical modelling input and results, post reaction XRD, and a table of E1056mR core elemental content.

9. REFERENCES

Alemu, B.L., Aagaard, P., Munz, I.A., Skurtveit, E., 2011. Caprock interaction with CO2: A laboratory study of reactivity of shale with supercritical CO2 and brine. Applied Geochemistry, 26(12): 1975-1989.

Armitage, P.J. et al., 2010. Diagenetic and sedimentary controls on porosity in Lower Carboniferous fine-grained lithologies, Krechba field, Algeria: A petrological study of a caprock to a carbon capture site. Marine and Petroleum Geology, 27(7): 1395-1410.

Bethke, C.M., Yeakel, S., 2012. The Geochemist's Workbench (Version 9.0): Reaction modeling guide. Aqueous Solutions, LLC, Champaign, Ill., 96 p.

Carroll, S.A., McNab, W.W., Torres, S.C., 2011. Experimental Study of Cement - Sandstone/Shale - Brine - CO2 Interactions. Geochemical Transactions, 12(1): 1-19.

707 Carroll, S.A., McNab, W.W., Dai, Z., Torres, S.C., 2013. Reactivity of Mount Simon sandstone
708 and the Eau Claire shale under CO 2 storage conditions. Environmental Science and
709 Technology, 47(1): 252-261.

710 Dávila, G., Luquot, L., Soler, J.M., Cama, J., 2016. Interaction between a fractured marl caprock
711 and CO2-rich sulfate solution under supercritical CO2 conditions. International Journal
712 of Greenhouse Gas Control, 48: 105-119.

713 Dawson, G.K.W. et al., 2015. Achieving Risk and Cost Reductions in CO2 Geosequestration
714 through 4D Characterisation of Host Formations, University of Queensland, ANLEC
715 R&D.

716 Delany, J.M., Lundeen, S.R., 1989. The LLNL thermodynamic database. Lawrence Livermore
717 National Laboratory Report UCRL-21658.

718 Ellis, B. et al., 2013. Dissolution-Driven Permeability Reduction of a Fractured Carbonate
719 Caprock. Environmental Engineering Science, 30(4): 187-193.

720 Ellis, B. et al., 2011. Deterioration of a fractured carbonate caprock exposed to CO2-acidified
721 brine flow. Greenhouse Gases: Science and Technology, 1(3): 248-260.

722 Farquhar, S.M., Dawson, G.K.W., Esterle, J.S., Golding, S.D., 2013. Mineralogical
723 characterisation of a potential reservoir system for CO2 sequestration in the Surat Basin.
724 Australian Journal of Earth Sciences, 60(1): 91-110.

725 Farquhar, S.M. et al., 2015. A fresh approach to investigating CO2 storage: Experimental CO2-
726 water-rock interactions in a freshwater reservoir system. Chemical Geology,
727 399(Measuring and predicting the geochemical impacts of CO2 storage on reservoir
728 rocks): 98-122.

729 Fischer, S., Liebscher, A., De Lucia, M., Hecht, L., 2013. Reactivity of sandstone and siltstone
730 samples from the Ketzin pilot CO2 storage site-Laboratory experiments and reactive
731 geochemical modeling. Environmental Earth Sciences, 70(8): 3687-3708.

732 Garcia-Rios, M., Luquot, L., Soler, J.M., Cama, J., 2015. Influence of the flow rate on
733 dissolution and precipitation features during percolation of CO2-rich sulfate solutions
734 through fractured limestone samples. Chemical Geology, 414: 95-108.

735 Glezakou, V.-A., Peter McGrail, B., Todd Schaef, H., 2012. Molecular interactions of SO2 with
736 carbonate minerals under co-sequestration conditions: A combined experimental and
737 theoretical study. Geochimica et Cosmochimica Acta, 92(0): 265-274.

738 Golab, A. et al., 2015a. Milestone 1.4 Final report of RCA and SCAL data on plugs from West
739 Wandoan-1 Well, FEI Lithicon, Report for ANLEC R&D.

740 Golab, A. et al., 2015b. Milestone 2.9: Final report of digital core analysis results for plug
741 samples from West Wandoan-1 Well., FEI-Lithicon, Report for ANLEC R&D.

742 Golab, A. et al., 2015c. Milestone 5.7: Final report on geochemical reactivity studies of core
743 material using ScCO2, Lithicon FEI, Report for ANLEC R&D.

744 Golab, A. et al., 2014. Technical report for Sub-project 5: Undertake time series (4D) imaging
745 and conventional experimental studies to measure geochemical reactivity and dissolution
746 trapping capacity of core material using supercritical CO2, Lithicon Australia Report for
747 ANLEC R&D.

748 Golab, A.N. et al., 2010. 3D porosity and mineralogy characterization in tight gas sandstones.
749 The Leading Edge, 29(12): 1476-1483.

750 Hangx, S., van der Linden, A., Marcelis, F., Bauer, A., 2013. The effect of CO2 on the
751 mechanical properties of the Captain Sandstone: Geological storage of CO2 at the
752 Goldeneye field (UK). International Journal of Greenhouse Gas Control, 19(0): 609-619.
753 Higgs, K.E., Haese, R.R., Golding, S.D., Schacht, U., Watson, M., 2015. The Pretty Hill
754 Formation as a natural analogue for CO2 storage; an investigation of mineralogical and
755 isotopic changes associated with sandstones exposed to low, intermediate and high CO2
756 concentrations over geological time. Chemical Geology, 399(Measuring and predicting
757 the geochemical impacts of CO2 storage on reservoir rocks): 36-64.
758 Jacquemet, N., Pironon, J., Saint-Marc, J., 2008. Mineralogical Changes of a Well Cement in
759 Various H2S-CO2(-Brine) Fluids at High Pressure and Temperature. Environmental
760 Science & Technology, 42(1): 282-288.
761 Jung, H.B., Um, W., Cantrell, K.J., 2013. Effect of oxygen co-injected with carbon dioxide on
762 Gothic shale caprock–CO2–brine interaction during geologic carbon sequestration.
763 Chemical Geology, 354(0): 1-14.
764 Karamalidis, A.K. et al., 2013. Trace Metal Source Terms in Carbon Sequestration
765 Environments. Environmental Science & Technology, 47(1): 322-329.
766 Kirste, D.M., Pearce, J.K., Golding, S., Frank, A., 2015. Reactive transport modelling of CO2
767 with SO2 and O2 as impurities for geological storage: Upscaling from the benchtop to the
768 reservoir, Goldschmidt, Prague, CZ.
769 Knackstedt, M. et al., 2013. Petrophysical Characterization Of Unconventional Reservoir Core
770 At Multiple Scales. Petrophysics, 54(03): 216-223.
771 Last, G.V., Schmick, M.T., 2011. Identification and Selection of Major Carbon Dioxide Stream
772 Compositions. PNNL-20493, Pacific Northwest National Laboratory.

773 Lu, J., Mickler, P.J., Nicot, J.-P., Yang, C., Darvari, R., 2016. Geochemical impact of O2
774 impurity in CO2 stream on carbonate carbon-storage reservoirs. International Journal of
775 Greenhouse Gas Control, 47: 159-175.
776 Lu, J., Mickler, P.J., Nicot, J.-P., Yang, C., Romanak, K.D., 2014. Geochemical impact of
777 oxygen on siliciclastic carbon storage reservoirs. International Journal of Greenhouse Gas
778 Control, 21: 214-231.
779 Luquot, L., Gouze, P., Niemi, A., Bensabat, J., Carrera, J., 2016. CO2-rich brine percolation
780 experiments through Heletz reservoir rock samples (Israel): Role of the flow rate and
781 brine composition. International Journal of Greenhouse Gas Control, in press.
782 Marcon, V., Kaszuba, J.P., 2015. Carbon dioxide–brine–rock interactions in a carbonate
783 reservoir capped by shale: Experimental insights regarding the evolution of trace metals.
784 Geochimica et Cosmochimica Acta, 168: 22-42.
785 Navarre-Sitchler, A.K. et al., 2013. Porosity and surface area evolution during weathering of two
786 igneous rocks. Geochimica et Cosmochimica Acta, 109(0): 400-413.
787 Palandri, J.L., Kharaka, Y.K., 2005. Ferric iron-bearing sediments as a mineral trap for CO2
788 sequestration: Iron reduction using sulfur-bearing waste gas. Chemical Geology, 217(3-
789 4): 351-364.
790 Pearce, J.K. et al., 2015a. SO2 Impurity Impacts on Experimental and Simulated CO2-Water-
791 Reservoir Rock Reactions at Carbon Storage Conditions. Chemical Geology,
792 399(Measuring and predicting the geochemical impacts of CO2 storage on reservoir
793 rocks): 65-86.

794 Pearce, J.K., Law, A.C.K., Dawson, G.K.W., Golding, S.D., 2015b. SO2-CO2 and pure CO2
795 reactivity of ferroan carbonates at carbon storage conditions. Chemical Geology,
796 10.1016/j.chemgeo.2015.07.001.
797 Pearce, J.K., Dawson, G.K.W., Law, A.C.K., Biddle, D., Golding, S.D., 2016. Reactivity of
798 micas and cap-rock in wet supercritical CO2 with SO2 and O2 at CO2 storage conditions.
799 Applied Geochemistry, 72: 59-76.

800 Porter, R.T.J., Fairweather, M., Pourkashanian, M., Woolley, R.M., 2015. The range and level of
801 impurities in CO2 streams from different carbon capture sources. International Journal of
802 Greenhouse Gas Control, 36(0): 161-174.
803 Ruhl, A.S., Kranzmann, A., 2013. Investigation of corrosive effects of sulphur dioxide, oxygen
804 and water vapour on pipeline steels. International Journal of Greenhouse Gas Control,
805 13(0): 9-16.
806 Schaef, H.T. et al., 2014. Mineralization of Basalts in the CO2–H2O–SO2–O2 System.
807 Environmental Science & Technology, 48(9): 5298-5305.
808 Schaef, H.T., McGrail, B.P., Owen, A.T., Arey, B.W., 2013. Mineralization of basalts in the
809 CO2–H2O–H2S system. International Journal of Greenhouse Gas Control, 16(0): 187-
810 196.
811 Shao, H., Kukkadapu, R.K., Krogstad, E.J., Newburn, M.K., Cantrell, K.J., 2014. Mobilization
812 of metals from Eau Claire siltstone and the impact of oxygen under geological carbon
813 dioxide sequestration conditions. Geochimica et Cosmochimica Acta, 141: 62-82.
814 Smith, M.M., Sholokhova, Y., Hao, Y., Carroll, S.A., 2013. Evaporite Caprock Integrity: An
815 Experimental Study of Reactive Mineralogy and Pore-Scale Heterogeneity during Brine-
816 CO2 Exposure. Environmental Science & Technology, 47(1): 262-268.

817 Talman, S., 2015. Subsurface geochemical fate and effects of impurities contained in a CO2
818 stream injected into a deep saline aquifer: What is known. International Journal of
819 Greenhouse Gas Control, 40: 267-291.
820 Wilke, F.D.H., Vásquez, M., Wiersberg, T., Naumann, R., Erzinger, J., 2012. On the interaction
821 of pure and impure supercritical CO2 with rock forming minerals in saline aquifers: An
822 experimental geochemical approach. Applied Geochemistry, 27(8): 1615-1622.
823 Wunsch, A., Navarre-Sitchler, A.K., Moore, J., Ricko, A., McCray, J.E., 2013. Metal release
824 from dolomites at high partial-pressures of CO2. Applied Geochemistry, 38: 33-47.
825 Wunsch, A., Navarre-Sitchler, A.K., Moore, J., McCray, J.E., 2014. Metal release from
826 limestones at high partial-pressures of CO2. Chemical Geology, 363: 40-55.
827 Xu, T.F., Apps, J.A., Pruess, K., Yamamoto, H., 2007. Numerical modeling of injection and
828 mineral trapping Of CO2 with H2S and SO2 in a sandstone formation. Chemical
829 Geology, 242(3-4): 319-346.
830
831
832
833
834
835
836
837
838

Figure 1. Experimental Schematic, where V = reaction vessel, DA = data acquisition box, ISCO = injection pump.

Figure 2. QEMSCAN images from sub-plug polished sections before reaction of a) Precipice Sandstone P1217m, b) Evergreen Formation E1056m, c) E1043m - note the purple areas correspond to barite in this sub-plug, d) E981m, e) Hutton Sandstone H800m, f) mineral color key.

Figure 3. SEM images of Precipice Sandstone a) – d) P1217m, e) – f) P1065m. a) surface view pre-reaction, inset K-sulphates and Na-carbonates (image width 500 μm), b) surface view post reaction, c) kaolin with bright traces of calcite pre-reaction and inset Na-carbonate (image width 100 μm), d) kaolin post reaction with calcite dissolved, e) kaolin pre reaction, inset Ti-oxide (image width 50μm) f) kaolin post-reaction with some removal of booklets. Qu = quartz, Su = sulphate, Ka = kaolinite, Ca = calcite, Ru = rutile.

Figure 4. Vertical planes from 3D micro-CT tomograms of sub-plugs of a) E1056m pre-reaction, b) E1056mR post-reaction, c) E1056m difference image where dark areas show loss of material or density, d) E981m pre-reaction, b) E981mR post-reaction, c) E981m difference image where dark areas show loss of material or density.

Figure 5. SEM images of Evergreen Formation sample E1056m. a) Surface pre-reaction with quartz (Qu), rutile (Ru), and calcite (Ca), b) view in a post-reaction with calcite dissolved

862 revealing pore filling clay (C), c) K-feldspar (KF) grain surrounded by calcite, d) view in c post-
863 reaction with residual pore filling clay (c) and bright barite (Ba) crystals inset magnified view of
864 barite (image width 30 μm), e) lithic grain pre-reaction, f) lithic grain post-reaction and inset Ca-
865 sulphate precipitated in the reactor (image width 200 μm).
866
867 Figure 6. SEM images of Evergreen Formation sample E1043m. a) Fe-rich Chlorite (Ch),
868 kaolinite (Ka), sphalerite (Sp) and albite (Al) pre-reaction, b) view in a post-reaction with
869 corrosion and coating by fine-grained precipitates, c) albite surface pre-reaction, d) albite surface
870 post reaction with precipitated booklets on surface and inset K-feldspar (image width 40 μm), e)
871 barite (Ba) and monazite (M) with a phosphate (P) rim (containing U and Th), and f) post
872 reaction with the phosphate rim corroded.
873
874 Figure 7. SEM images of Evergreen Formation sample E981m. a) surface view pre-reaction
875 with sandy layer above and fine-grained siltstone layer below, lighter areas are mixed fine-
876 grained ankerite (An) and chlorite (Ch), dark areas are organic matter (Co), bright grain is zircon
877 (Zr) b) surface view post reaction with ankerite corroded and fine layer of precipitates, c)
878 labradorite (La) grain pre-reaction, d) labradorite grain corroded post-reaction with inset fluffy
879 clay precipitates and bright barite (Ba) (image width 40 μm).
880
881 Figure 8. SEM images of Hutton Sandstone sample H800m. a) surface view pre-reaction with
882 calcite (Ca) cemented quartz (Qu) grains and coal lamination (Co), b) surface view post reaction
883 with calcite cement corroded and precipitated gypsum (Gy) crystals, c) bright phosphate (P) pre-
884 reaction with La and Ce signatures, d) view in c post-reaction with small cubic precipitates (CP),

885 e) EDS of precipitated gypsum, f) photograph of core block post-reaction with yellow coloration
886 and covered in gypsum needles.

887

888 Figure 9. Selected water chemistry during gas-brine-rock reactions. a) solution pH, b) dissolved
889 Ca concentration (mg/kg), c) dissolved Fe concentration, d) dissolved Al concentration.

890

891

892

893 Table 1. Mineral contents (area %) as determined by QEMSCAN of a polished sub-plug slice pre and post
894 (R) reaction.

	P1217m	P1217mR	P1165m[1]	P1165mR	E1056m	E1056mR	E1043m	E1043mR	E981m	E981mR	H800m	H800mR
Depth / m	1217.48	1217.48	1165.44	1165.44	1056.1	1056.1	1043.7	1043.7	981.24	981.24	800.83	800.83
Quartz	97.1	97.9	na	95.1	25.0	28.1	61.0	53.5	34.4	38.5	41.4	45.8
Alkali feldspar	0.0	0.0	na	0.0	13.0	10.6	3.4	4.4	3.7	3.3	6.2	8.3
Plagioclase	0.0	0.0	na	0.0	17.7	20.3	22.3	32.7	9.9	8.7	6.2	8.9
Muscovite/ Illite	0.2	0.3	na	0.4	0.4	6.0	2.3	1.1	1.2	4.7	2.1	2.5
Biotite	0.0	0.0	na	0.0	0.0	2.2	1.2	0.6	6.5	1.0	0.3	0.0
Illite-Smectite	0.0	0.0	na	0.0	11.9	8.7	0.0	0.0	22.5	17.0	0.0	0.0
Kaolinite	2.4	1.7	na	4.2	0.9	1.9	2.8	3.5	2.4	6.9	3.9	12.3
Chlorite	0.0	0.0	na	0.0	0.9	1.5	3.8	1.5	7.6	2.0	0.6	1.8
Calcite	0.0	0.0	na	0.0	25.2	16.0	0.5	0.0	0.0	0.0	36.7	18.5
Apatite			na				0.1	0.1	0.1	0.0	0.1	0.0
Barite							0.2	0.2				

Gypsum/anhydrite			na								0.0	0.0[2]
Rutile	0.1			0.1								
Unclassified and traces	0.2	0.1	na	0.2	4.9	4.7	2.2	2.3	11.8	17.8	2.4	1.8
Total	100.0	100.0	na	99.9	99.9	100.0	100.0	100.0	99.8	99.9	99.9	100.0
Total Clay/Mica	2.4	2.0	na	4.6	14.1	18.1	10.1	3.7	40.2	31.6	6.9	16.6

[1] No result for P1165m sample lost in transit, [2] Trace gypsum quantified ~ 0.02

Table 2. Properties derived from segmentation of sub-plug images as 3D vol % a) pre-reaction, and b) post-reaction (R) change calculated from the pre and post reaction images.

Table 2a

Sample	Depth / m	Total porosity	Grain matrix	Clay content	Framework grain content	Heavy mineral content
P1217m	1217.48	20.9		5.7	73.3	0.1
P1165m	1165.44	19.4		6.6	73.8	0.1
E1056m	1056.10	4.4	23.2		75.7	0.6
E1043m	1043.70	6.3	67.4		27.2	2.7
E981m	981.24	8.3	89.2		7.3	2.3(chlorite)
H800m	800.83	3.8	24.3	11.8	63.5	0.2

Table 2b

Sample	Depth / m	Change after reaction
P1217mR	1217.48	0 [1]
P1165mR	1165.44	0 [1]
E1056mR	1056.10	9.1
E1043mR	1043.70	3.5
E981mR	981.24	3.0
H800mR	800.83	3.7

[1] Little discernible change, very small changes are likely clay movement, and for P1165mR some minor loss of high density material possibly siderite.

905 Table 3a Rock core composition by fusion and ICPOES as % oxide, loss on ignition (LOI), and 3b minor
906 and trace elemental content (mg/kg) by digestion and ICPMS (note Detection limit DL reported in
907 µg/kg).

	SiO_2	TiO_2	AL_2O_3	Fe_2O_3	MnO	MgO	CaO	Na_2O	K_2O	P_2O_5	LOI	Total
P1165m	98.30	0.11	1.54	0.03	0.00	0.00	0.03	0.12	0.07	0.03	0.82	101.04
P1217m	97.42	0.06	1.11	0.04	0.00	0.00	0.00	0.21	0.57	0.03	1.25	100.64
E1056m	57.56	0.50	12.82	2.33	0.61	0.44	12.01	2.00	2.32	0.14	11.03	101.76
E1043m	73.15	1.24	12.25	3.03	0.05	0.54	1.97	2.41	1.85	0.21	2.75	99.45
E981m	68.91	0.78	16.25	4.43	0.03	0.83	0.69	1.40	2.00	0.14	4.83	100.30
H800m	51.69	0.30	6.52	1.01	0.42	0.14	20.95	0.82	1.25	0.07	18.28	101.44

908

909 Table 3b

Sample	Li	Be	B	P	Sc	Ti	V	Cr	Co	Ni	Cu	Zn
P1217m	2.3	0.1	21.1	35.2	0.4	305.6	3.4	4.3	2.9	1.1	16.0	4.9
P1165m	2.2	0.1	30.1	36.8	0.7	563.4	3.8	2.7	1.0	2.1	12.8	7.5
E1056m	36.4	1.6	51.2	679.4	4.6	3062.9	60.5	22.2	9.6	8.5	16.4	52.3
E1043m	21.7	1.2	22.1	808.4	8.8	7459.1	61.3	37.9	13.7	13.5	20.9	77.7
E981m	45.7	2.7	43.0	493.2	10.4	3903.4	68.9	34.8	6.7	10.6	18.7	72.0
H800m	8.6	0.8	20.9	231.0	4.1	1793.4	20.3	14.1	4.5	5.8	4.8	32.5
DL (µg/kg)	3.5E-02	1.9E-03	5.9E-01	1.4E+00	3.9E-03	7.9E-02	7.0E-02	2.4E-01	9.6E-04	4.3E-03	2.4E-02	2.4E-02

910

911

Sample	As	Se	Rb	Sr	Zr	Nb	Mo	Cd	Sn	Ba	Pb	U
P1217m	0.6	0.1	1.8	8.7	18.2	109.9	0.1	0.0	2.2	25.6	3.3	0.3
P1165m	1.0	0.1	3.1	8.4	32.0	233.6	0.1	0.0	2.4	24.3	5.2	0.4
E1056m	3.5	0.4	99.3	282.3	117.0	761.6	0.4	0.1	1.4	535.7	14.0	1.5
E1043m	12.4	0.5	60.6	319.9	219.6	1545.0	1.1	0.2	1.7	1140.4	15.5	2.1
E981m	4.6	0.8	93.7	203.1	204.3	1275.9	0.9	0.3	3.0	479.5	17.6	2.6
H800m	1.7	0.3	54.4	191.5	104.1	600.0	0.2	0.1	0.9	375.4	9.9	0.9
DL(ppb)	4.2E-02	3.4E-02	6.5E-03	7.3E-03	2.6E-03	1.2E-01	4.9E-03	6.8E-04	6.1E-03	7.1E-03	5.7E-04	6.7E-04

912

913 Table 4a: Major and minor dissolved elements, pH and conductivity (cond.) during reactions (mg/kg). DL
914 is detection limit, and ND is no data.

	Time (h)	pH	Cond. (mS/cm)	Al	B	Ba	Ca	Co	Cr	Cu	Fe
P1217m	0	5.11	3.03	0.49	1.24	0.07	4.80	0.32	0.00	3.86	1.22
	72	1.75	11.14	2.38	1.42	0.16	6.33	0.40	3.81	7.45	21.97
	216	1.69	10.75	4.05	1.31	0.08	3.44	0.46	4.25	7.48	24.76

	384	1.70	10.15	1.98	1.18	0.06	2.91	0.45	2.74	7.31	21.43
	552	1.65	10.47	2.67	1.23	0.07	3.43	0.43	1.38	7.40	16.59
	696	1.81	10.61	2.83	1.27	0.07	3.09	0.43	1.19	7.45	16.17
P1165m	0	4.29	2.79	0.07	0.10	0.04	1.11	0.03	0.33	2.32	2.03
	144	1.24	12.82	1.31	0.14	0.07	3.54	0.07	0.77	4.18	8.30
	240	1.05	13.06	5.29	0.32	0.18	5.10	0.34	15.68	10.50	74.54
	408	1.16	14.37	2.98	0.24	0.08	2.06	0.19	3.28	4.74	22.30
	576	1.24	33.90	5.26	0.36	0.09	2.50	0.35	9.94	5.27	44.24
	672	1.17	13.06	5.55	0.28	0.08	2.37	0.31	6.16	4.52	38.74
E1056m	0	7.55	6.46	0.81	ND	2.54	249.15	0.02	<DL	0.11	<DL
	72	5.66	8.02	1.11	ND	0.43	891.53	0.15	0.05	0.15	7.21
	168	5.46	5.17	1.31	ND	0.33	944.48	0.16	0.02	0.11	<DL
	408	7.52	18.23	2.82	ND	0.24	964.33	0.23	<DL	0.11	<DL
	576	7.65	ND	2.31	ND	0.25	1053.30	0.65	<DL	0.12	<DL
	624	6.25	44.40	1.10	ND	0.27	1155.85	0.69	0.07	0.08	5.43
E1043m	0	5.49	2.92	<DL	0.08	0.06	6.23	0.01	0.11	0.03	0.66
	120	1.80	6.33	22.07	0.04	0.06	103.09	0.46	21.42	0.47	155.18
	216	2.03	5.27	34.89	0.11	0.06	251.14	0.85	22.95	0.67	195.42
	288	2.18	5.07	32.42	0.14	0.04	300.82	1.07	21.56	0.68	164.32
	384	2.25	5.50	32.75	0.18	0.04	358.41	1.31	15.04	0.81	135.06
	456	2.45	5.19	28.00	0.17	0.04	345.45	1.82	11.20	0.68	140.08
	552	2.37	7.84	23.27	0.14	0.03	309.55	2.56	18.84	1.09	243.32
	648	2.33	5.27	25.26	0.17	0.04	366.83	1.91	7.58	1.22	108.90
E981m	0	6.25	15.60	<DL	<DL	<DL	4.27	0.03	0.07	<DL	2.77
	120	1.92	7.85	19.04	<DL	0.06	103.10	0.17	1.73	0.23	93.88
	216	2.20	6.28	39.08	<DL	0.02	188.84	0.33	2.89	0.34	164.21
	288	2.14	6.66	44.89	<DL	<DL	217.60	0.37	2.22	0.35	151.08
	384	2.32	6.42	45.19	<DL	<DL	239.21	0.41	1.83	0.44	130.55
	624	2.30	3.29	46.91	<DL	<DL	262.44	0.46	1.41	0.60	91.84
H800m	0	6.42	3.65	1.14	0.34	0.37	301.94	0.21	0.02	0.01	0.05
	72	5.61	4.84	0.70	0.41	0.18	832.23	0.68	0.04	0.26	39.23
	216	5.68	5.03	0.47	0.13	0.11	921.88	0.43	0.00	<DL	4.15
	384	5.95	5.31	0.34	0.18	0.11	1039.00	0.40	0.03	0.02	0.34
	552	5.76	5.52	0.37	0.21	0.12	1024.73	0.27	0.02	0.02	0.08
	696	5.86	5.40	0.66	0.35	0.11	965.08	0.42	<DL	0.06	0.12
Blank	672	1.46	14.93	2.21	<DL	<DL	<DL	0.03	1.74	0.01	17.30
DL				1.0E-02	6.9E-03	1.1E-04	5.1E-03	6.7E-04	3.4E-03	1.6E-03	8.8E-04

915

916 Table 4b: Major and minor dissolved elements during reactions (mg/kg).

	Time (h)	K	Li	Mg	Mn	Na	Ni	S	Si	Sr	Ti	Zn
P1217m	0	154.39	0.00	0.65	0.28	554.89	2.22	71.74	6.22	0.04	0.00	4.20
	72	170.28	0.00	1.27	0.40	596.05	3.32	605.47	11.15	0.05	0.07	4.36
	216	171.72	0.00	1.29	0.52	566.26	4.22	555.11	6.86	0.04	0.04	0.52
	384	195.15	0.01	1.14	0.48	590.95	4.14	549.64	7.39	0.04	0.02	0.54
	552	175.42	0.01	1.32	0.36	560.72	2.91	547.15	8.04	0.04	0.02	0.51
	696	173.14	0.00	1.18	0.33	561.83	2.64	544.62	8.57	0.04	0.03	0.63
P1165m	0	22.26	0.00	0.17	0.08	694.59	0.52	10.10	0.85	0.01	<DL	0.18
	144	22.65	0.00	0.40	0.20	748.97	0.96	793.79	2.40	0.06	0.01	0.30
	240	ND	0.01	0.81	1.02	ND	7.15	ND	8.95	0.05	0.07	1.24
	408	23.05	0.00	0.30	0.23	548.93	2.08	749.20	5.40	0.02	0.02	0.40
	576	28.38	0.00	0.37	0.62	761.71	5.54	836.93	9.22	0.03	0.02	0.51
	672	21.69	0.00	0.34	0.49	516.28	4.46	746.47	9.23	0.03	0.02	0.52
E1056m	0	6844.58	ND	2.56	9.50	126.44	0.14	5.18	2.50	3.27	ND	0.06
	72	6111.36	ND	5.33	40.15	119.44	1.55	403.21	5.36	4.11	ND	0.25
	168	6143.35	ND	6.42	41.87	117.61	1.65	384.71	9.61	4.02	ND	0.26
	408	4517.22	ND	6.64	44.43	117.64	5.38	351.03	7.95	3.72	ND	0.37
	576	5475.64	ND	7.63	51.81	137.37	28.14	350.41	9.87	4.11	ND	0.43
	624	7309.10	ND	9.43	57.69	116.29	29.19	386.79	12.35	4.78	ND	0.52
E1043m	0	8.22	0.01	0.31	0.25	444.46	0.39	1.02	1.60	0.26	0.00	0.03
	120	13.22	0.09	11.20	4.61	473.02	8.54	306.01	28.64	2.50	0.01	0.70
	216	24.80	0.18	22.8	9.19	826.23	9.02	727.8	59.35	5.70	0.83	1.51

				7				9				
	288	28.71	0.19	25.25	11.30	894.87	12.46	682.31	65.27	6.37	0.01	1.55
	384	30.62	0.22	30.31	14.55	936.17	16.93	766.77	72.10	7.37	0.02	1.94
	456	27.18	0.19	28.77	17.29	870.14	35.03	708.03	69.79	6.93	0.01	1.80
	552	22.97	0.18	25.80	20.66	765.12	63.89	613.23	62.36	6.04	0.02	1.67
	648	29.64	0.21	30.68	18.91	856.75	37.73	606.09	68.65	6.88	0.02	3.03
E981m	0	23.40	<DL	0.44	0.04	620.76	0.22	17.55	3.68	0.24	<DL	<DL
	120	49.44	0.23	13.15	3.47	848.66	1.68	594.12	56.66	5.38	<DL	1.10
	216	73.02	0.23	25.91	6.87	1009.69	3.03	640.04	91.34	8.86	<DL	2.45
	288	74.79	0.32	30.22	7.68	1032.60	2.73	668.62	101.73	9.97	<DL	2.86
	384	72.73	0.33	34.81	8.81	1005.63	2.43	633.65	101.53	10.16	<DL	3.56
	624	70.86	0.37	39.71	9.90	1038.88	2.33	647.06	102.59	10.25	<DL	4.13
H800m	0	4.52	0.01	2.04	8.13	570.19	11.71	21.08	5.92	0.60	0.02	5.72
	72	5.61	0.01	3.59	30.15	561.39	30.71	421.16	11.44	1.25	0.03	4.22
	216	8.14	0.02	2.85	29.47	565.58	15.20	306.51	4.14	1.46	<DL	0.18
	384	8.27	0.03	3.12	32.07	643.49	12.37	311.09	5.56	1.68	<DL	0.45
	552	9.67	0.03	3.28	30.44	614.57	5.13	288.26	6.37	1.70	<DL	0.22
	696	7.64	0.07	3.43	30.70	586.43	12.35	284.50	6.56	1.64	0.03	0.31
Blank	672	2.79	0.01	<DL	0.12	575.03	1.10	722.32	0.94	0.01	0.01	<DL
DL		2.7E-01	7.1E-05	2.1E-02	1.5E-04	2.7E-01	1.9E-03	1.8E-03	3.0E-02	4.3E-05	9.4E-04	1.0E-03

917

918

919 Table 5: Dissolved trace P during reactions (µg/kg). DL is detection limit and ND is no data.

920

	Time (h)	P
P1217m	0	ND
	72	ND
	552	<DL
	696	<DL
P1165m	0	73.79
	144	608.54
	672	ND
E1043m	0	970.18
	120	ND
	384	37.74
	648	ND
H800m	0	ND
	72	ND
	552	<DL
	696	<DL
Blank	672	11.72
DL		3.8E+00

921

922 Table A1: Analytical methods applied to the core samples and experimental waters reported in this
923 manuscript and supplementary information. R indicates where a method was also applied to the core
924 after reaction. Perm = permeability. Whole rock = rock fusion, digestion and LOI. T = analysis without
925 filtering, for total metals. [1] Sub-plug was lost in transit. [2] ICPMS was not performed owing to the higher
926 salinity, a whole rock digestion and XRD of only this core post reaction was performed instead. GWB =
927 geochemical modelling. Additionally porosimetry, XRD and petrography of adjacent core sections
928 referred to in this manuscript are in Dawson et al., 2015.

	P1217m	P1165m	E1056m	E1043m	E981m	H800m
Micro-CT	X	X	X	X	X	X
Micro-CT R	X	X	X	X	X	X
QEMSCAN	X	[1]	X	X	X	X
QEMSCAN R	X	X	X	X	X	X
SEM-EDS	X	X	X	X	X	X
SEM-EDS R	X	X	X	X	X	X
N_2 Perm	X					X
N_2 Perm R	X					X
Brine perm	X	X	X	X	X	X

Brine perm R	X	X		X		X
Whole rock	X	X	X	X	X	X
ICPOES	X	X	X	X	X	X
ICPOES T			X	X	X	
IC, pH, Cond	X	X	X	X	X	X
ICPMS	X	X	[2]	X	X	X
GWB	X	X	X	X	X	X

929

930

931

932

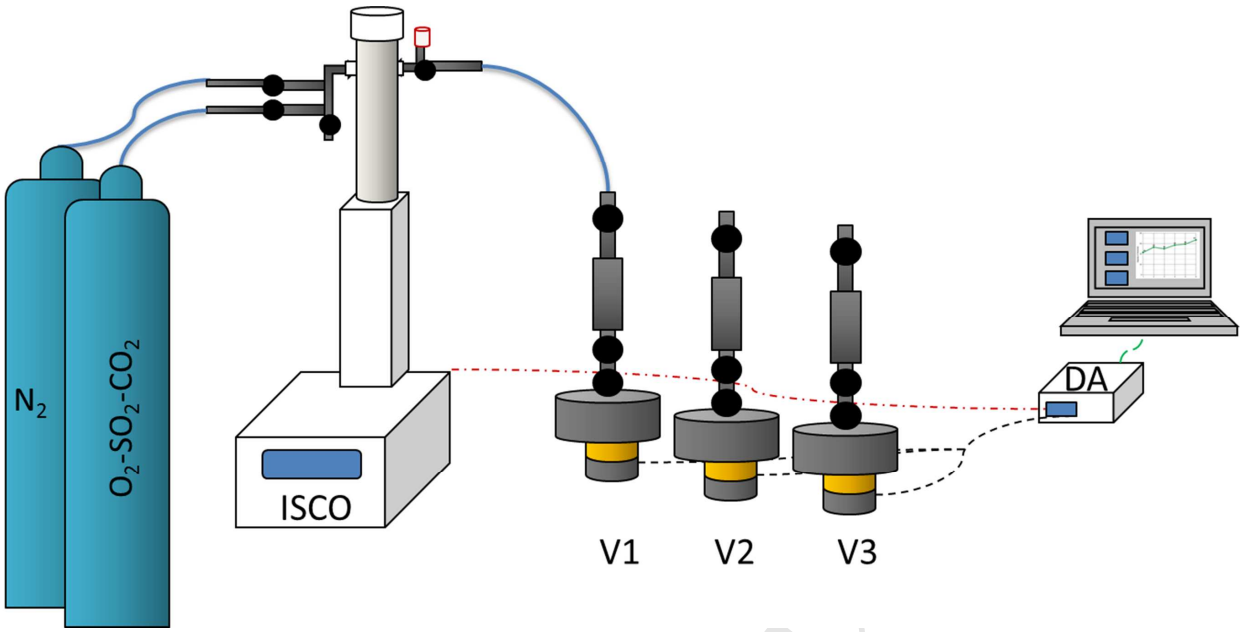

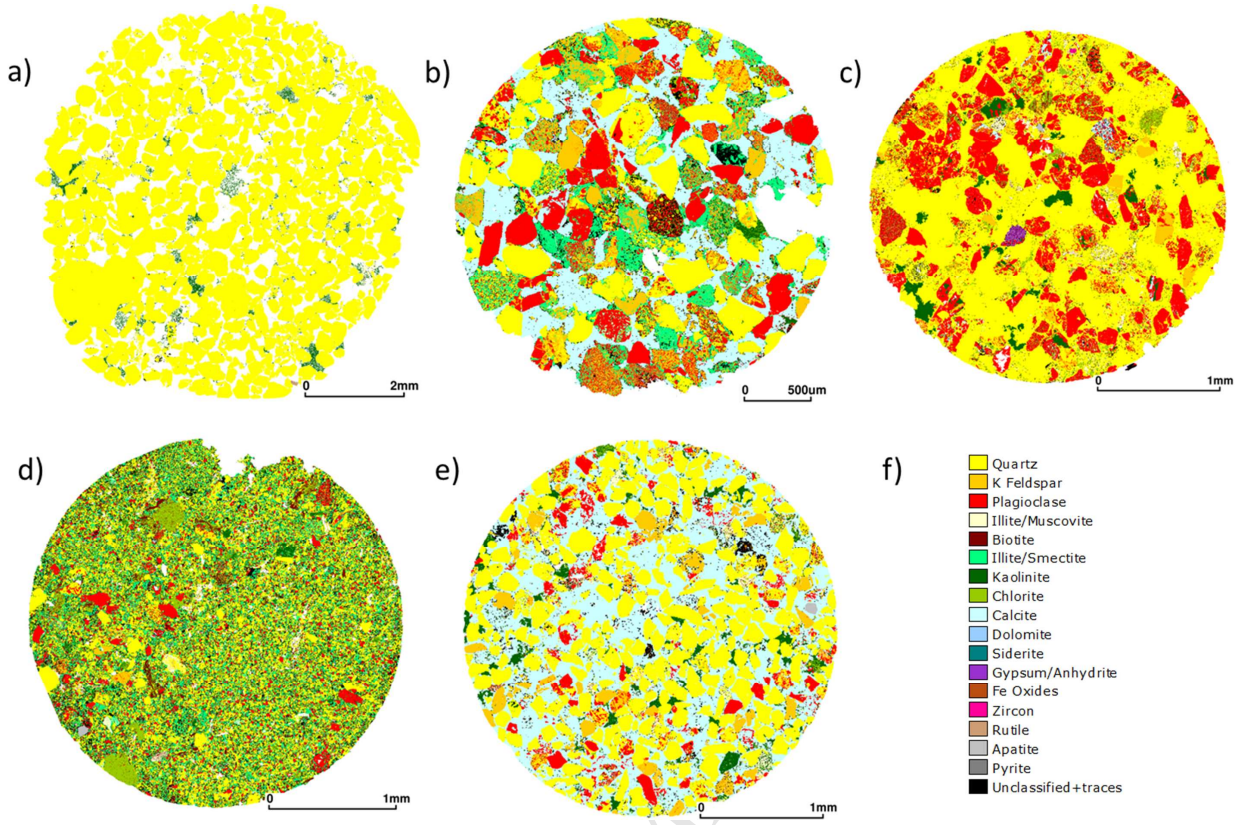

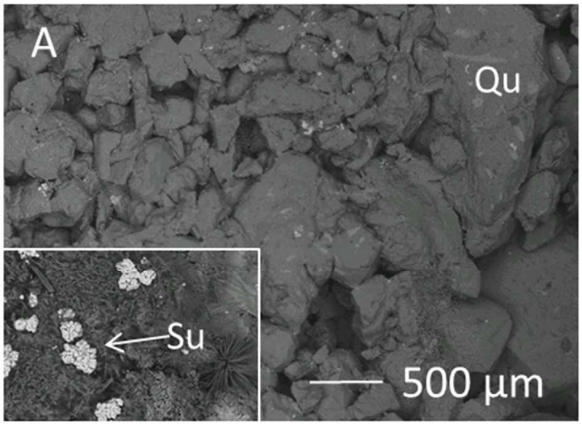
A
Qu
Su
500 µm

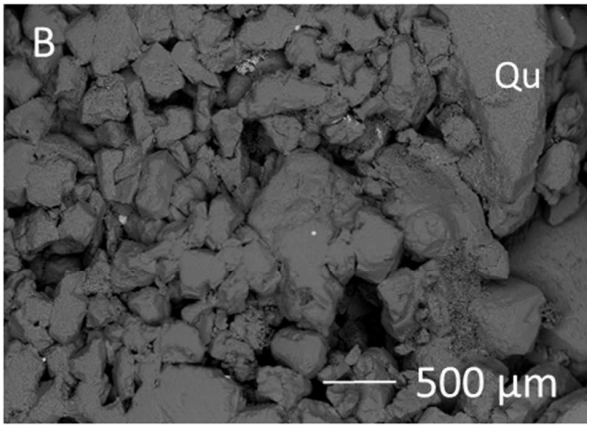
B
Qu
500 µm

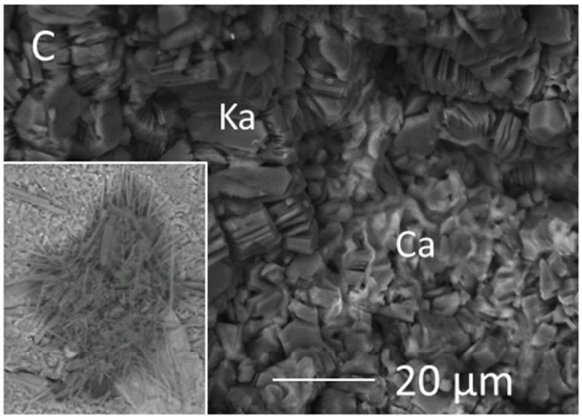
C
Ka
Ca
20 µm

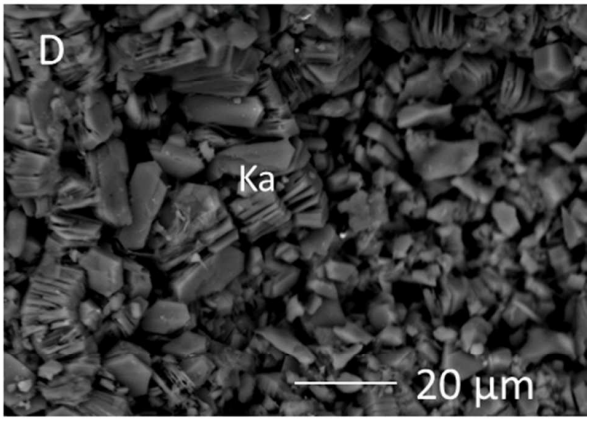
D
Ka
20 µm

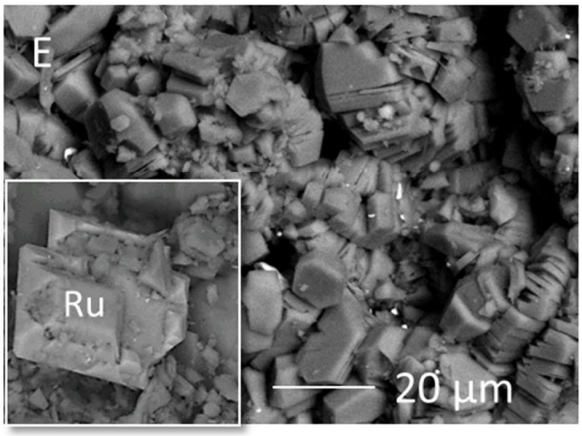
E
Ru
20 µm

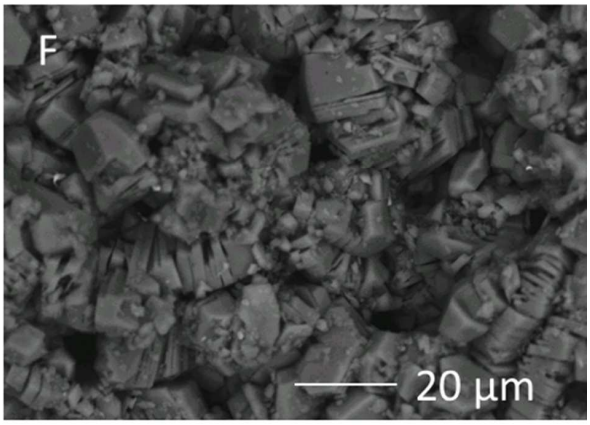
F
20 µm

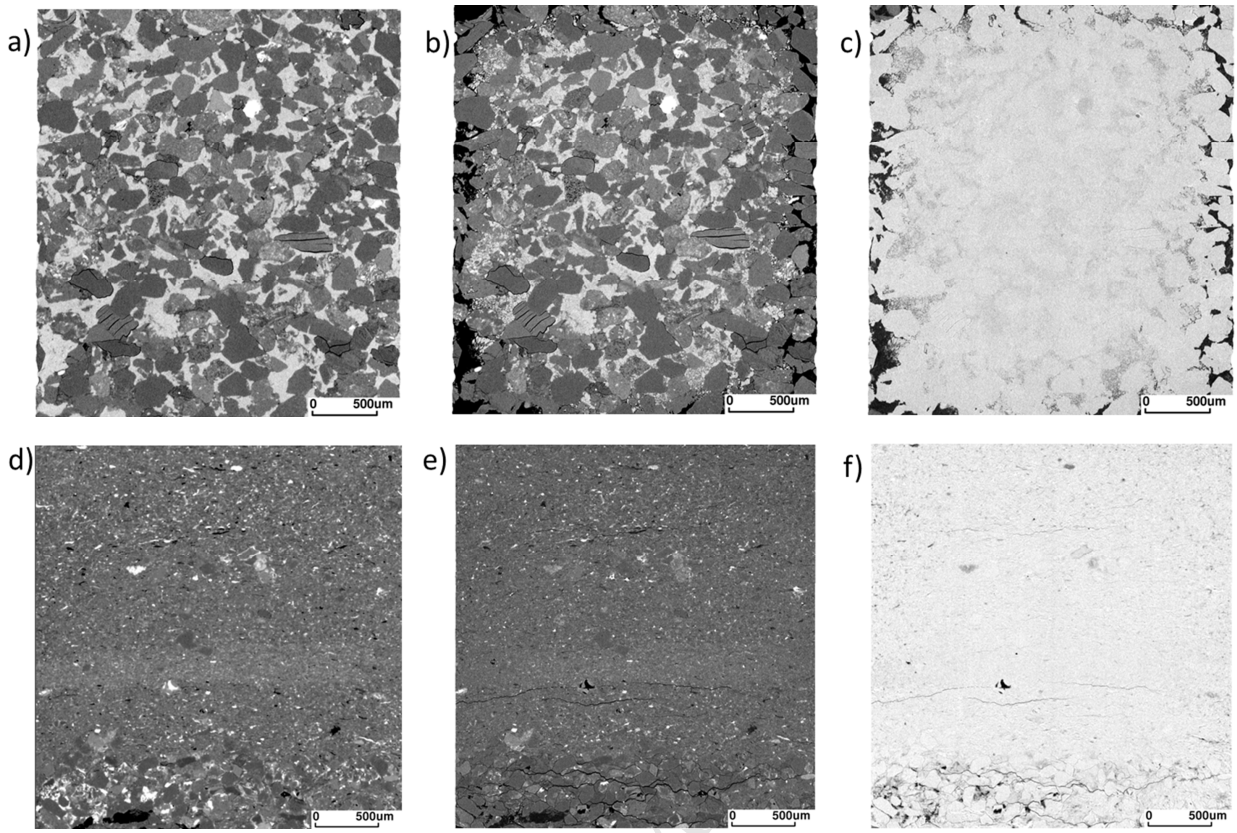

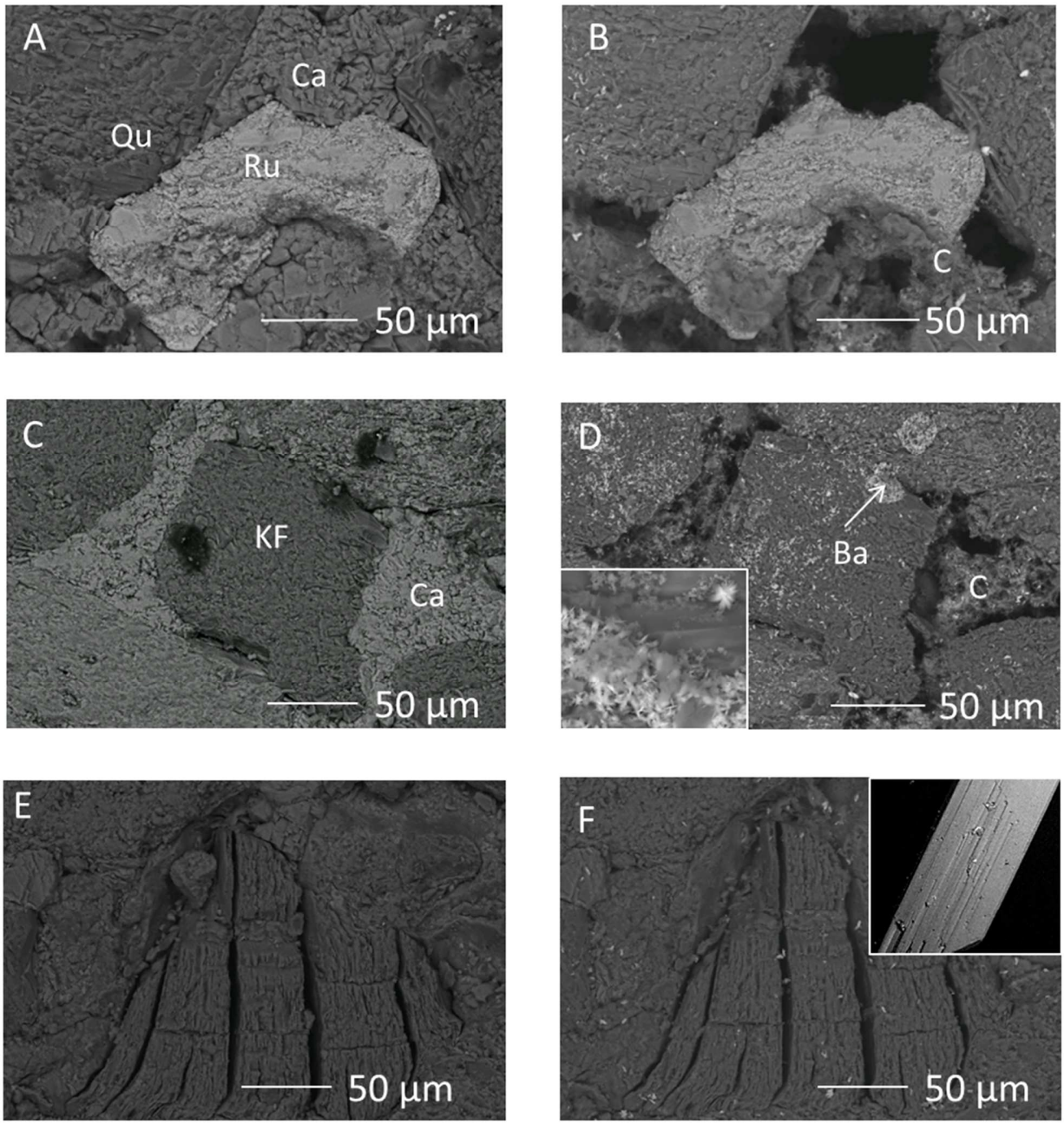
A
Ca
Qu
Ru
50 µm
B
C
50 µm
C
KF
Ca
50 µm
D
Ba
C
50 µm
E
50 µm
F
50 µm

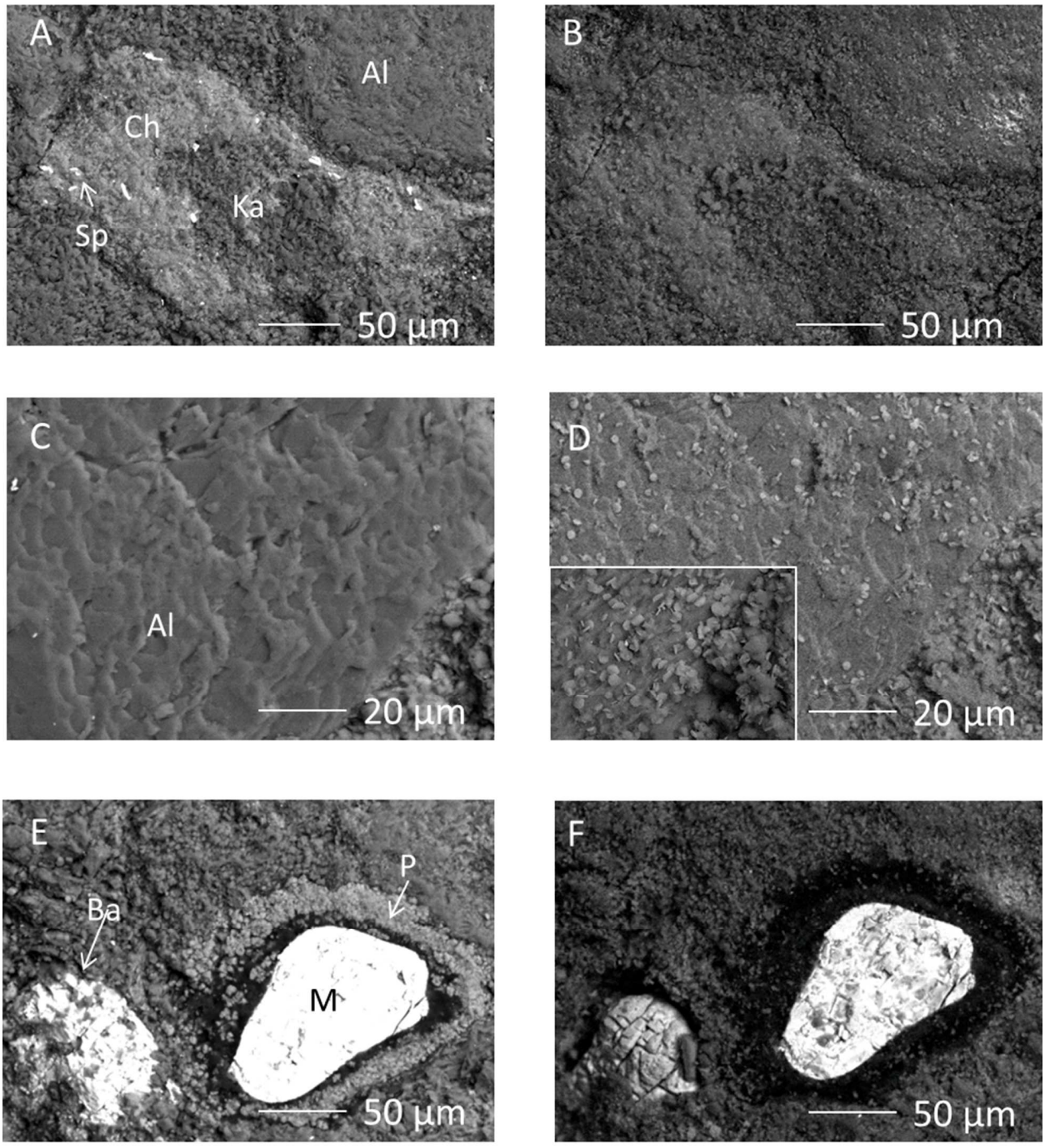
A
Al
Ch
Ka
Sp
50 µm
B
50 µm
C
Al
20 µm
D
20 µm
E
P
Ba
M
50 µm
F
50 µm

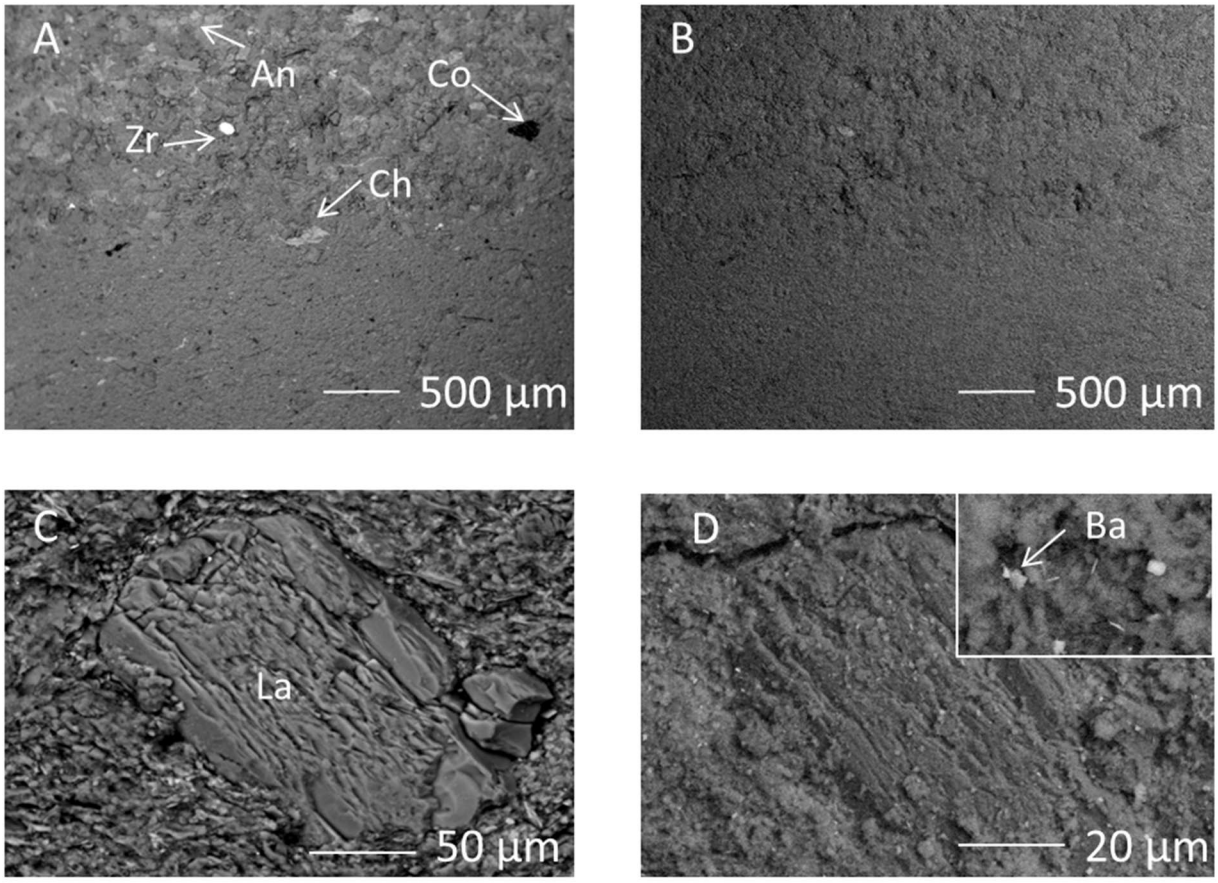

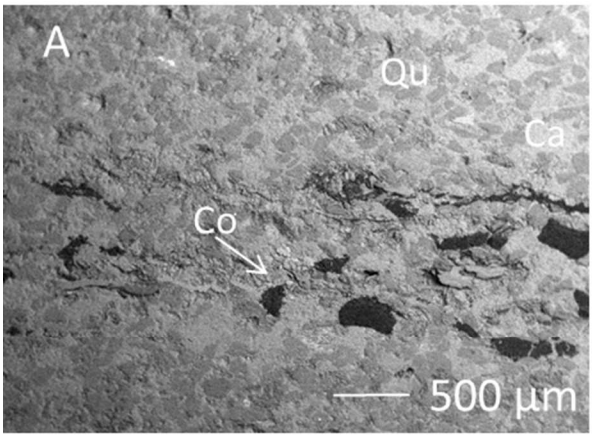
A
Qu
Ca
Co
500 µm

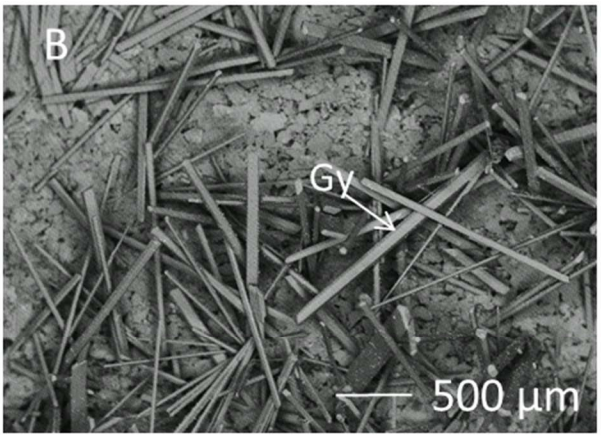
B
Gy
500 µm

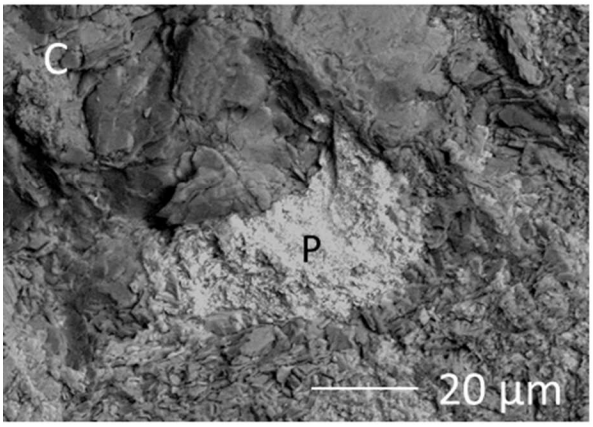
C
P
20 µm

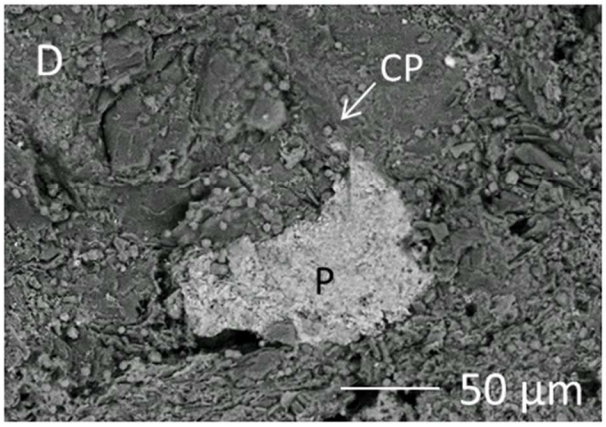
D
CP
P
50 µm

E

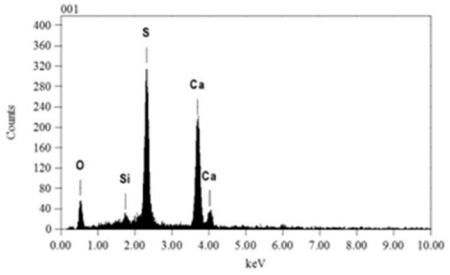
001
Counts
keV
O
Si
S
Ca
Ca

F


1 cm

A

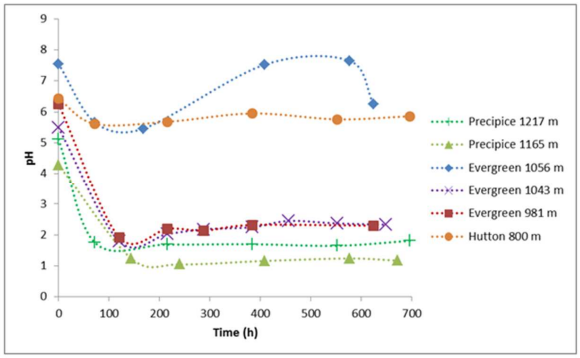

B

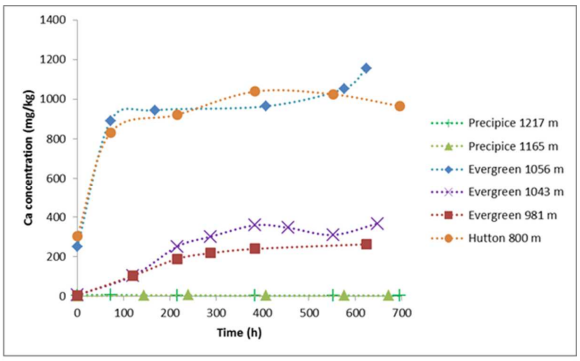

C

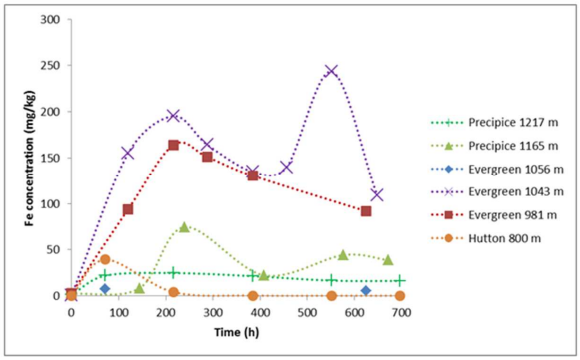

D

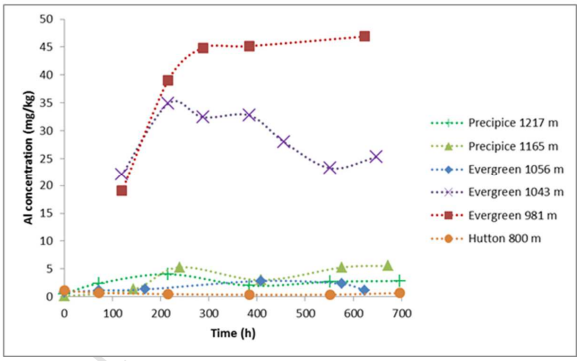

Highlights

- O_2-SO_2-CO_2 experiments on CO_2 sequestration site reservoir and cap-rock cores.
- Coupled micro CT and geochemical characterisation before and after reactions.
- Strong acidification with reservoir core, no change in porosity.
- Formation of open porosity in calcite cemented core, with buffered pH.
- Dissolved Mn, Mg, Co, Zn correlated with Ca from carbonates in cap-rocks.